



## CorteXpert: A model-based method for automatic renal cortex segmentation



Dehui Xiang<sup>a</sup>, Ulas Bagci<sup>b</sup>, Chao Jin<sup>a</sup>, Fei Shi<sup>a</sup>, Weifang Zhu<sup>a</sup>, Jianhua Yao<sup>c</sup>, Milan Sonka<sup>d,e,f</sup>, Xinjian Chen<sup>a,\*</sup>

<sup>a</sup>School of Electronics and Information Engineering, Soochow University, Jiangsu 215006, China

<sup>b</sup>Center for Research in Computer Vision, University of Central Florida (UCF), Orlando, FL 32816, USA

<sup>c</sup>Department of Radiology and Imaging Sciences, National Institute of Health, Bethesda, MD 20892, USA

<sup>d</sup>Department of Electrical and Computer Engineering, the University of Iowa, Iowa City, IA 52242, USA

<sup>e</sup>Department of Ophthalmology and Visual Sciences, the University of Iowa, Iowa City, IA 52242, USA

<sup>f</sup>Department of Radiation Oncology, the University of Iowa, Iowa City, IA 52242, USA

### ARTICLE INFO

#### Article history:

Received 29 July 2016

Revised 17 May 2017

Accepted 22 June 2017

Available online 23 August 2017

#### Keywords:

Cortex model adaptation

Non-uniform graph search

Renal cortex

### ABSTRACT

This paper introduces a model-based approach for a fully automatic delineation of kidney and cortex tissue from contrast-enhanced abdominal CT scans. The proposed framework, named *CorteXpert*, consists of two new strategies for kidney tissue delineation: cortex model adaptation and non-uniform graph search. *CorteXpert* was validated on a clinical data set of 58 CT scans using the cross-validation evaluation strategy. The experimental results indicated the state-of-the-art segmentation accuracies (as dice coefficient):  $97.86\% \pm 2.41\%$  and  $97.48\% \pm 3.18\%$  for kidney and renal cortex delineations, respectively.

© 2017 Elsevier B.V. All rights reserved.

### 1. Introduction

Kidney cancer is a life-threatening disease with a high mortality rate and poor prognosis all over the world, with 338000 new cases diagnosed in 2012 (Ferlay et al., 2013). Renal cell carcinoma, which arises from the renal cortex, is the most common type of kidney cancer in adults, responsible for approximately 80% of cases (Garcia et al., 2009). There is a lot of evidence to show that partial nephrectomy has become the first treatment of selective renal tumors, with equivalent oncological cure and better preservation of renal function compared to radical nephrectomy (Russo and Huang, 2008; Clark et al., 2011; Shao et al., 2012). To achieve the best resection plan, surgeons need to identify the location of the kidney portion that would be cut off. Renal transplantation is also a well-recognized treatment method than hemodialysis. Radiological evaluation of potential kidney donors is required to identify patients with kidneys that function well (Muto et al., 2011; Yano et al., 2012; Kato et al., 2011).

Since volumetric kidney and cortex measurements are correlated with the functionality of the kidneys, the pre- and post-

operation non-invasive measurements of kidney and cortex volumes are clinically important and need a careful evaluation. The segmentation plays a key role in employing these evaluations, particularly renal cortex volume because it is a better predictor for determining kidney functionality. However, there are several challenges in kidney and renal cortex segmentation. First, the internal structures of kidneys are complex and difficult to recognize, as shown in Fig. 1(a). Briefly, kidneys contain four major internal structures: cortex, column, medulla, and pelvis. Renal cortex is connected with the renal column, and its shape can be considered as complex because its inner boundaries are non-smooth and locally non-convex. Second, there are several neighboring tissues or organs, e.g., renal column, muscles, and liver, with similar intensities. This leads to low contrast and blurred boundaries in CT images between renal cortex and nearby structures. Therefore, renal cortex segmentation using conventional methods such as region growing may easily leak into its neighbors. Third, image artifacts and noise may easily affect the segmentation process. Renal cortex segmentation can be disturbed by different gray value intervals between renal tissues and artifacts. To address these problems, prior information (in the form of appearance, shape, or hybrid) can be used to separate adjacent organs even with similar intensities (Chen et al., 2009; 2010a,b; 2012a,b; Li et al., 2012; Xiang et al., 2011; Li et al., 2015; Ju et al., 2015). However, modeling shape of renal cortex is not a trivial task because the anatomy

\* Corresponding author.

E-mail addresses: [xiangdehui@suda.edu.cn](mailto:xiangdehui@suda.edu.cn) (D. Xiang), [bagci@crvc.ucf.edu](mailto:bagci@crvc.ucf.edu) (U. Bagci), [shifei@suda.edu.cn](mailto:shifei@suda.edu.cn) (F. Shi), [wfzhu@suda.edu.cn](mailto:wfzhu@suda.edu.cn) (W. Zhu), [jyao@mail.nih.gov](mailto:jyao@mail.nih.gov) (J. Yao), [milan-sonka@uiowa.edu](mailto:milan-sonka@uiowa.edu) (M. Sonka), [xjchen@suda.edu.cn](mailto:xjchen@suda.edu.cn) (X. Chen).

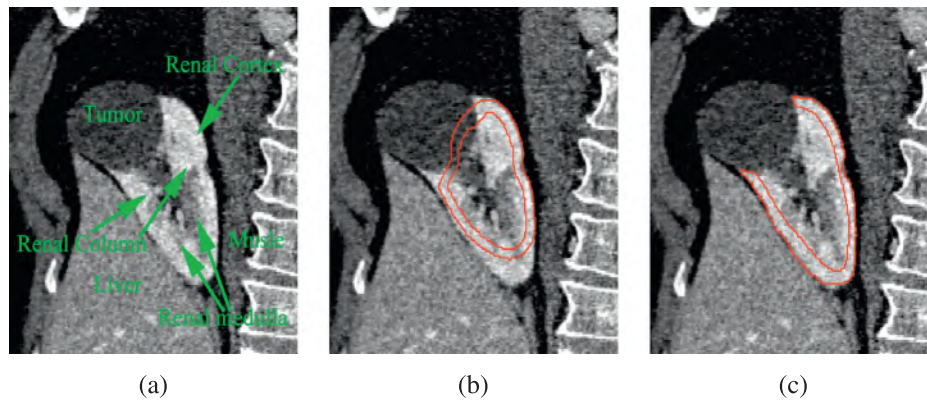


Fig. 1. Renal cortex segmentation. (a) A CT Slice; (b) Initial segmented renal cortex; (c) Final segmented renal cortex by our method.

of the renal cortex varies largely in different healthy individuals, both in shape and size. Besides, tumor and other pathologies can change the anatomical structure of renal cortex significantly. In this paper, we propose a novel shape model-based segmentation framework to address the aforementioned challenges in the segmentation module of the renal surgery planning. The proposed framework is a coarse-to-fine segmentation process (*CorteXpert*) that consists of three parts: model construction (Part I), initialization (Part II), and segmentation (Part III). First, a two-layer statistical shape model is constructed based on the point distribution model (PDM) for the purpose of integrating shape variation into the segmentation process as a shape prior. Then, one of the layers is used to locate the kidney *roughly* in the CT image. Automatic renal cortex model adaptation is performed progressively in the space spanned by the eigenvectors computed by principal component analysis (PCA) of the PDM. In the delineation part, the multi-scale first order partial derivative boundary function is used to define “true boundaries” of renal cortex integrated with a non-uniform graph search (NUGS) method by utilizing local intensity distribution. The presented framework improves our initial approach (Chen et al., 2012a; Li et al., 2012), which can be considered as the state-of-the-art system. Summary of the presented framework’s steps is the following.

- First, we use a precise clinical definition of the renal cortex, which many studies fail to do. Although the renal column and the cortex are functionally two different compartments, they have similar intensity distribution. In our implementation, we use two-layer statistical shape models to separate renal columns from cortex during the model construction.
- Second, we initialize the localization algorithm for the outer and the inner layers of the renal cortex. In our new initialization algorithm, less number of iteration is required for convergence and the overall initialization system is less sensitive to perturbations, as shown in Fig. 1(b).
- Third, our algorithm is different from the registration/atlas-based methods where registration may likely fail in the local minimum of the distance function, and the computational cost is huge. Instead, we develop a purely delineation-based algorithm, which is not only accurate but also extremely efficient.
- Fourth, to capture non-uniform intensity distribution that leads to better delineation performance, we introduce a non-uniform graph search approach. Nodes of the graph are non-equidistantly and adaptively sampled according to the initial surface and the non-uniform intensity distribution. The multi-scale boundary responses of first order partial derivatives are used to compute the weights of nodes for the outer surface detection. The filtered image is used to compute the weights of nodes for inner surface detection. Even in low contrast and

slender regions as shown in Fig. 1(c), our proposed algorithm is still highly accurate and robust in detecting and delineating the kidney and its compartments.

## 2. Related work

There are several studies in the literature for kidney and renal cortex segmentation using CT and MR images, including both semi-automatic (de Priester et al., 2001; Shen et al., 2009; Chevaillier et al., 2008; Boykov et al., 2001; Rusinek et al., 2007; Sun et al., 2004; Song et al., 2008; Padigala et al., 2009; Chen et al., 2009; Shim et al., 2009) and fully automatic methods (Ali et al., 2007; Zöllner et al., 2009; Tang et al., 2010). For kidney segmentation in dynamic MR images, not only the spatial information but also the time intensity curves (TIC) were used. Shen et al. (2009) presented a semi-automatic kidney segmentation method based on the morphological 3D h-maxima transform from MR images. Similarly, Chevaillier et al. (2008) proposed a semi-automated split and merge method based on TIC. Boykov et al. (2001) and Rusinek et al. (2007) developed a temporal Markov model to describe the TIC for each pixel followed by the min-cut algorithm. Although the performance was at a clinically acceptable level, specifying the seed points for the kidney segmentation made it impractical due to sensitivity in seed localizations. For registration-based methods, Sun et al. (2004) presented an image registration algorithm to delineate the renal cortex for dynamic renal perfusion MR images. Another registration-based approach (Zöllner et al., 2009) separated the inner compartments of kidney by k-means clustering after a non-rigid registration. Lately, Song et al. (2008) presented a 4D level set framework for dynamic MR images kidney segmentation. The method combined information from spatial anatomical structures and temporal dynamics. Despite all the progress in MR image processing for renal analysis, CT scan is still considered to be the clinical standard for the quantification of renal diseases.

Previous investigations (Shen et al., 2009; Boykov et al., 2001; Ali et al., 2007; Tang et al., 2010; Zöllner et al., 2009) considered renal cortex and column as a single tissue type in images although they are functionally and anatomically different. To make a strict definition of the renal cortex, it would be a good choice to consider only the out-layer of the kidney as a cortex because the renal columns have anatomical and functional differences (Padigala et al., 2009). Chen et al. (2012a) used a pseudo-3D oriented active appearance model method to locate a kidney, and combined morphologic operations and an iterative shape constrained graph cut method are used to segment the renal cortex. Li et al. (2012) applied an implicit shape registration method to roughly initialize the whole kidney and then utilized multiple surface graph searching to detect the renal cortex.

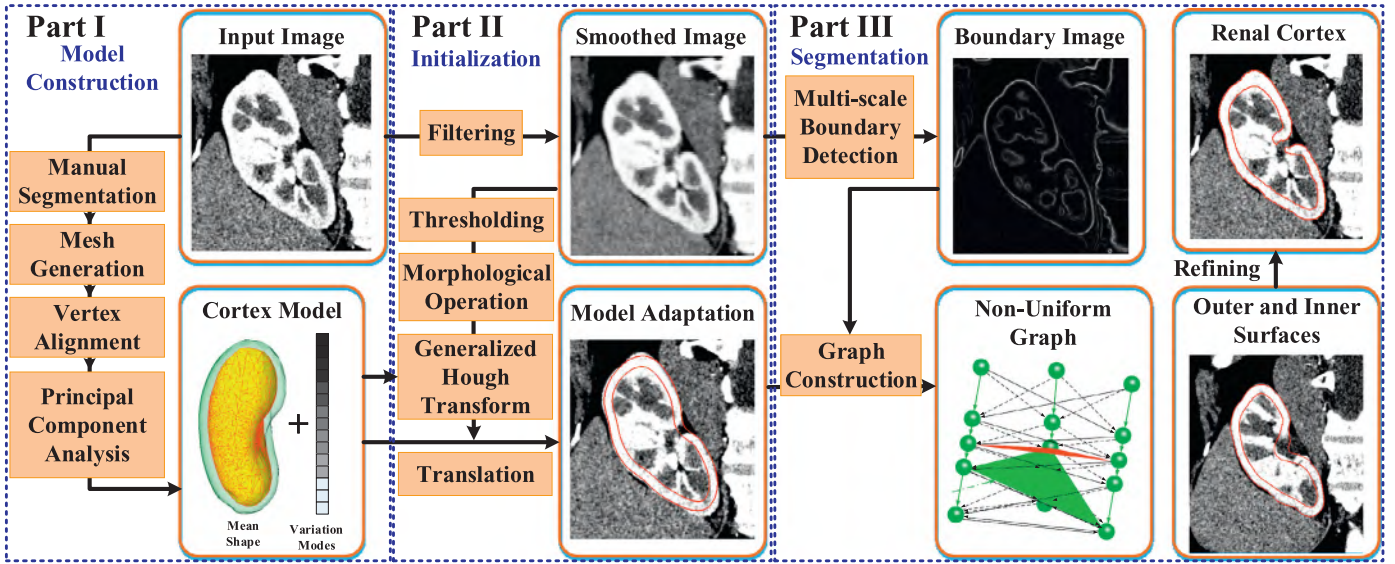


Fig. 2. The proposed *corteXpert* framework.

### 3. Method

Fig. 2 shows the flowchart of the proposed method. In the shape model construction part, two surfaces of the renal cortex are segmented manually in training images, and these shapes are used to build PDMs. In the initialization part, the renal cortex is localized by applying the generalized Hough transform (GHT) and the cortex model adaptation method. In the segmentation part, a non-uniform multiple surface graph is constructed to obtain the final renal cortex segmentation. The details of each part are given in the following sub-sections.

#### 3.1. Part I: Model construction

A priori knowledge can be learned from a representative set of training images along with different meshes from different subjects. The derived information can then be associated with the meshes to automatically segment volume of interests. An important issue thus is to establish surface correspondence between the training meshes. However, adapting two uncalibrated meshes with some motions such as significant rotation and scale changes still remains a challenging problem. Although semi-automatic or fully automatic landmark generation methods (Dryden and Mardia, 1998; Davies et al., 2002) can be employed, numerous limitations exist. For these reasons, both the outer and the inner layers of the renal cortex are manually labeled with two non-overlapped regions in a slice-by-slice manner. The labeled binary images are converted into triangulated meshes using the marching cube algorithm (Lorenson and Cline, 1987) for representing both the outer and the inner layer surfaces. The minimum description length (MDL) algorithm by Heimann et al. (2006) is next used to establish a vertex correspondence between the reference meshes for both the outer and the inner layers (Fig. 3). In MDL, a conformal parameterization function is used to describe the vertex distribution on the training shapes. Next, vertex positions are modified locally without disturbing established correspondences through a gradient descent optimization employed for minimization of the MDL cost. To reduce the time complexity of the MDL process, all meshes are simplified using the quadric error metric (Hoppe, 1999) with the same  $\nabla$  vertices connected in  $\mathbb{T}$  triangles as shown in Fig. 3.

To establish vertex correspondence for both surface layers of different renal cortex shapes, meshes need to be aligned in a Cartesian coordinate system via similarity transformation.

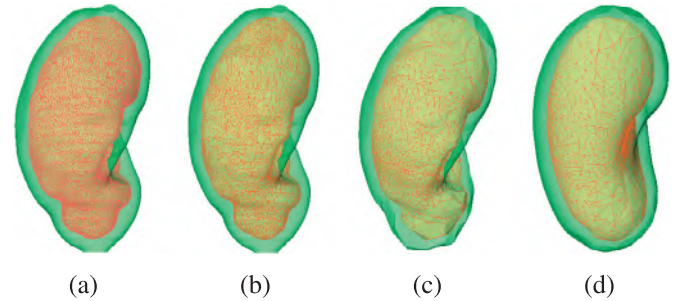


Fig. 3. Renal cortex model construction. (a) A manually segmented renal cortex. (b) A simplified mesh of a manually segmented renal cortex based on quadric error metric. (c) Aligned renal cortex meshes using the minimum description length algorithm. (d) The mean shape of the renal cortex.

This also allows analysis of inter-patient and inter-phase shape variability. The similarity transformation in this case consists of three translation, three rotation, and one scaling parameter with a total of seven degrees of freedom in 3-D space ( $T_x$ ,  $T_y$ ,  $T_z$  are the three parameters translated along the three axes,  $\theta$ ,  $\varphi$ ,  $\omega$  are the three angles of rotation about three axes,  $s$  is the scaling parameter). The vertices on two corresponding meshes of the renal cortex can be expressed as a 1-D vector  $\mathbf{u} = (\mathbf{u}_o, \mathbf{u}_i)^T$ , where,  $\mathbf{u}_o = (x_{o1}, y_{o1}, z_{o1}, x_{o2}, y_{o2}, z_{o2}, \dots, x_{oN_o}, y_{oN_o}, z_{oN_o})$  are the vertex coordinates of the outer layer,  $\mathbf{u}_i = (x_{i1}, y_{i1}, z_{i1}, x_{i2}, y_{i2}, z_{i2}, \dots, x_{iN_i}, y_{iN_i}, z_{iN_i})$  are the vertex coordinates of inner layer,  $N_o$  and  $N_i$  are the number of vertices for outer and inner surfaces respectively ( $N_o = N_i$ ). Although the similarity transformation is done using the unit quaternion algorithm proposed by Horn (1987), other methods can also be used instead (Bagci et al., 2012).

Inter-patient and inter-phase shape variability of the outer layers and the inner layers can be learned from the consistent set of training meshes using PCA. The PDM can be used to describe shape variability. With the combination of similarity transformation, the resulting PDM can be expressed as

$$\Psi = T^{-1} \left( \bar{\Psi} + \sum_{m=1}^M \lambda_m \mathbf{p}_m \right), \quad (1)$$

where,  $\mathbf{p}_m$  is the principal mode of variation obtained through PCA.  $\lambda_m$  is the corresponding weight for each principal mode,  $T^{-1}$  is the inversion of similarity transformation for registered shape coord-

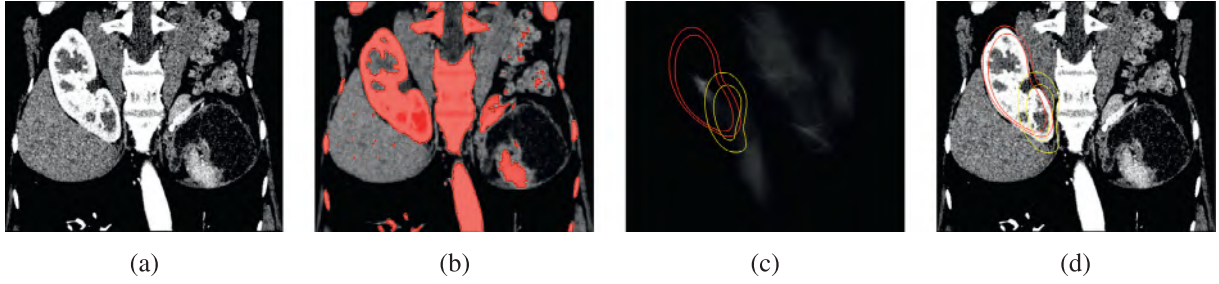


**Fig. 4.** Kidney Localization. (a) The original image; (b) The Gaussian filtered image with the thresholded image  $I_b$ ; (c) The resulting GHT image with mean renal cortex shape model (yellow curves) and translated mean renal cortex (red curves); (d) The original image with mean renal cortex shape model (yellow curves) and translated mean renal cortex shape model (red curves). (For interpretation of the references to colour in this figure legend, the reader is referred to the web version of this article.)

dinate system to the original coordinate system,  $\bar{\Psi}$  is the mean shape of the training set, and  $M$  is the number of variation modes. For the outer layer, the mean shape is computed by

$$\bar{\Psi}_o = \frac{1}{N_o} \sum_{k=1}^{N_o} T(\mathbf{u}_o^k), \quad (2)$$

where,  $\mathbf{u}_o^k$  is the 1-D vertex coordinate vector of the outer mesh of the  $k$ th training mesh. Similarly, the mean shape for the inner layer is computed by

$$\bar{\Psi}_i = \frac{1}{N_i} \sum_{k=1}^{N_i} T(\mathbf{u}_i^k). \quad (3)$$

where,  $\mathbf{u}_i^k$  is the 1-D vertex coordinate vector of the inner mesh of the  $k$ th training mesh. The mean mesh derived from the training set is shown in Fig. 3(d). The mean renal cortex shape can be represented as  $(\bar{\Psi}_o, \bar{\Psi}_i)$ .

### 3.2. Part II: Model initialization

Automatic localization of model assembly is not a trivial task for at least two reasons. (1) The inner surface of the renal cortex may not be simply created from the recognized kidney due to varying thickness levels of the renal cortex. (2) The number of vertices should not be too high to avoid suboptimal localization and segmentation.

#### 3.2.1. Image smoothing and kidney localization

Noise is inherent in medical images and needs to be minimized prior to image analysis tasks as shown in Fig. 4(a). In this study, we use Gaussian filtering (Whitaker and Xue, 2001). The intensity range of the output is normalized to  $[I_{\min}, I_{\max}] = [0, 255]$  as shown in Fig. 4(b).

For localization of model assembly, we use the generalized Hough transform (GHT) by Khoshelham (2007), which is proved to be a robust and powerful method for detecting any arbitrary shape in an image. In the GHT training process, the triangulated mesh of the average outer mesh is employed as a template shape in order to reduce the dimensionality of the parameter space. The gravity center  $\mathbf{c}$  is used as the reference point. For each vertex on the mean outer mesh  $\bar{\Psi}_o$ , the normal orientation can be represented as the azimuthal and revolution angles ( $\alpha$  and  $\beta$  respectively) of a spherical coordinate system, and the two angles are discretized as two entries reference table (look-up table) with the corresponding angle steps  $t_\alpha$  and  $t_\beta$ . The vector  $\mathbf{r}_p$  pointing from the mesh to the center is indexed by  $\alpha$  and  $\beta$ , and stored in the look-up table. For kidney localization, the thresholded image  $I_b$  is computed by  $[b(I_{\max} - I_{\min}) + I_{\min}, I_{\max}]$ . Since some adjacent tissues are similar to the kidney, morphological opening can be used to remove those small structures as shown in Fig. 4(b). Then the GHT voting

scores are computed according to the gradient of  $I_b$  as shown in Fig. 4(c). The normalized gradient is represented as the azimuthal and revolution angles ( $\alpha$  and  $\beta$  respectively) of a spherical coordinate system, and also the two angles are discretized as two entries reference table (look-up table) with the corresponding angle steps  $t_\alpha$  and  $t_\beta$ . The vector  $\mathbf{r}_p$  pointing from the curve point to the potential center is indexed by  $\alpha$  and  $\beta$ . The voting score of the potential center is increased. The mean renal cortex shape  $(\bar{\Psi}_o, \bar{\Psi}_i)$  is translated to the point with the maximal GHT voting score as shown in Fig. 4(c).

#### 3.2.2. Model adaptation

In model adaptation, we simply deform both layers of the PDM locally to match into the target boundaries. For this task, we utilize the idea of shape-constrained deformable models (Ecabert et al., 2008). Briefly, the two meshes are adapted to the boundaries of the renal cortex and the initial image from the outer mesh is matched to the thresholded image  $I_b$  in two alternating steps. In each iteration, the first step is the deformation of the outer layer mesh from the initial renal cortex by progressively detecting the candidate kidney boundary along the normal vertices so that the deformed outer layer mesh  $\Psi_o^\tau$  can be driven to the candidate kidney boundary  $\Psi_t$ . In the second step, the deformed outer layer mesh  $\Psi_o^\tau$  is registered to the mean outer layer model  $\bar{\Psi}_o$  so as to generate a PDM of renal cortex  $(\Psi_o^\lambda, \Psi_i^\lambda)$ , and then the PDM of the renal cortex is considered as initial renal cortex and constrains the deformation of  $(\Psi_o^\lambda, \Psi_i^\lambda)$  (initially the translated mean outer and inner layer meshes). This iterative process can be described as minimizing the distance  $D$  between the deformed meshes and the target boundary. The distance function can be defined as

$$D = D_{region} + \kappa D_{surface} \quad (4)$$

where,  $D_{region}$  denotes a region term, which measures the distance between  $\Psi_o^\tau$  and  $\Psi_t$  in the signed Euclidean distance field;  $\Psi_t$  represents the mesh converted from the thresholded image  $I_b$ ;  $D_{surface}$  denotes a boundary term which measures Euclidean distance between  $\Psi_o^\tau$  and  $\Psi_o^\lambda$ ;  $\Psi_t; \mathbf{v}$  represents the corresponding vertex on the  $\Psi_o^\tau$ ,  $\Psi_o^\lambda$  and  $\Psi_t$ ;  $\kappa$  controls the balance between the region and surface constraints.

##### A. Model Deformation

For each vertex  $\mathbf{v}_i$  on the outer layer mesh  $\Psi_o^\tau$ , the boundary candidate is searched along the normal vector  $\mathbf{n}_i$  of the vertex at discrete positions as

$$\mathbf{v}_{ij} = \mathbf{v}_i + j\delta\mathbf{n}_i, j = -n_m, \dots, -1, 0, 1, \dots, n_m \quad (5)$$

where  $\delta$  is the searching step which depends on the size of the kidney. It is computed according to the average length of edges, which connects the current vertex and its adjacent vertices. For vertex  $\mathbf{v}_i$ , the mean length  $l$  of adjacent edges is computed, and then the searching step  $\delta$  is set  $l$ . If vertex  $\mathbf{v}_i$  is inside the kidney (in the foreground of the binary image  $I_b$ ) and the vertex  $\mathbf{v}_{ij}$

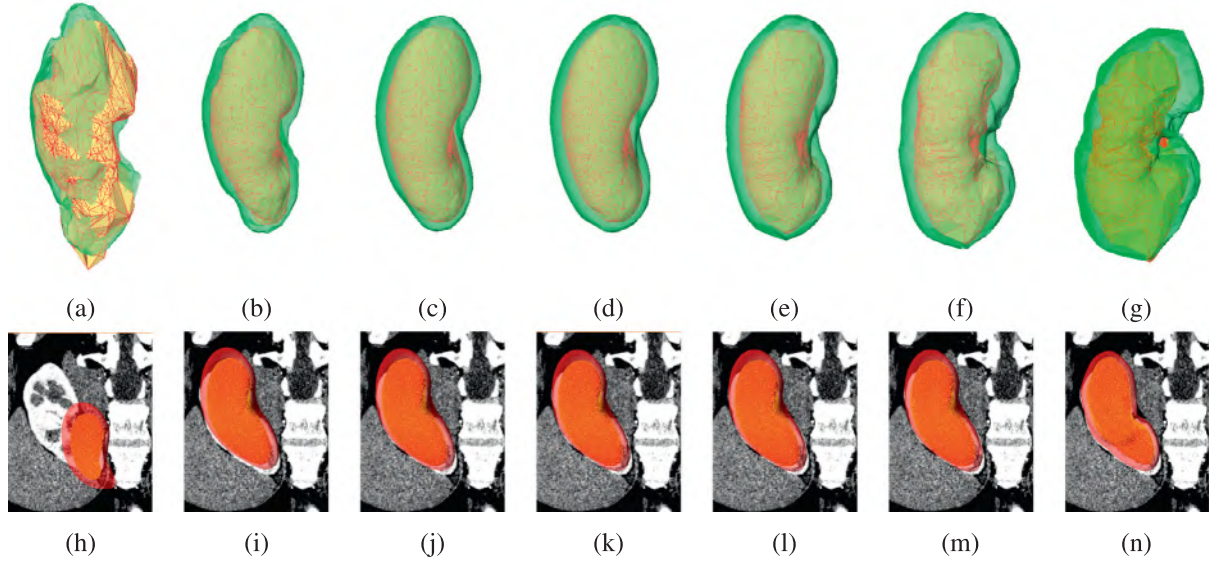


**Fig. 5.** Renal cortex model adaptation. (a) The generated renal cortex shape model with  $-2\sqrt{\lambda_m}$ ; (b) The generated renal cortex shape model with  $-\sqrt{\lambda_m}$ ; (c) The generated renal cortex shape model with  $-0.5\sqrt{\lambda_m}$ ; (d) The mean shape model of renal cortex; (e) The generated renal cortex with  $0.5\sqrt{\lambda_m}$ ; (f) The generated renal cortex shape model with  $\sqrt{\lambda_m}$ ; (g) The generated renal cortex shape model with  $2\sqrt{\lambda_m}$ . (h) The mean shape model of renal cortex in the test image; (i) The renal cortex shape model is moved based on the center of the segmented kidney using the GHT; (j)–(l) The renal cortex shape model is adapted in the test image after the 1st to 4th iterations in eigen-space; (l) The final outer and inner surfaces with model adaptation.

is searched along the normal vector  $n_i$  and  $j > n_t$ , and then  $\mathbf{v}_i$  is updated by  $\mathbf{v}_{ij}$ ; if vertex  $\mathbf{v}_i$  is outside the kidney (in the background of the binary image  $I_b$ ) and vertex  $\mathbf{v}_{ij}$  is searched along the inverse normal vector  $-n_i$  and  $|j| > n_t$ , and then  $\mathbf{v}_i$  is updated by  $\mathbf{v}_{ij}$ .  $n_m$  is the maximal searching number,  $n_t$  is a moving threshold value, describing kidney region detection and small structures can be neglected in order to improve the robustness to noise and non-kidney structures in the adjacent region.  $n_m$  depends on the voxel spacings and the distance between the initial outer layer mesh and the kidney boundary in the binary image  $I_b$ .

After the outer layer mesh  $\Psi_o^\tau$  is deformed, it is converted into a binary image  $I_o^\tau$ . The Euclidean distance transformation algorithm (Meijster et al., 2000) is used to compute the signed Euclidean distance field  $\Gamma_\tau$  for deformed mesh and  $\Gamma_t$  for the binary image  $I_b$ . The distance of mesh deformation can be computed by

$$D_{\text{region}} = \frac{1}{n_r} \sum_{\mathbf{q}} (\Gamma_\tau(\mathbf{q}) - \Gamma_t(\mathbf{q})) \quad (6)$$

where,  $n_r$  denotes a normalization parameter in the local region.  $\mathbf{q}$  represents a coordinate vector of a voxel in Euclidean distance field  $\Gamma$ ; In the implementation, the signed Euclidean distance fields  $\Gamma_\tau$  for deformed mesh and  $\Gamma_t$  for coarse boundary can be calculated locally for increased memory efficiency and decreased computation time.  $n_r$  is a normalization factor.

#### B. Parametric Adaptation

In the process of mesh deformation, the outer layer mesh  $\Psi_o^\tau$  may be far from the kidney boundary  $\Psi_t$ . The desirable boundaries may be near to surrounding organs; this may contribute to mesh deformation. To utilize the shape prior, parametric adaptation is employed to constrain the mesh deformation. In this condition, the vertex positions are free variables and can be represented as mean shape and shape variability. A renal cortex PDM ( $\Psi_o^\lambda, \Psi_i^\lambda$ ) is generated based on the mean shape and shape variability obtained from Eq. (1) and (2). This process can be expressed as

$$(\Psi_o^\lambda, \Psi_i^\lambda) = T^{-1} \left( \bar{\Psi}_o + \sum_{m=1}^M \lambda_m p_{o,m}, \bar{\Psi}_i + \sum_{m=1}^M \lambda_m p_{i,m} \right) \quad (7)$$

where,  $b_m$  is the weight of the principal mode  $\mathbf{p}_m$ .

At the beginning of the parametric adaptation, the deformed outer layer mesh  $\Psi_o^\tau$  is registered to the mean outer layer model  $\bar{\Psi}_o$  using the unit quaternion algorithm proposed by Horn (1987) and get similarity transformation parameters  $T$  and registered mesh  $T(\Psi_o^\tau)$ . The displacement  $\Delta\Psi_o^\tau$  is computed as

$$\Delta\Psi_o^\tau = T(\Psi_o^\tau) - \bar{\Psi}_o = \sum_{m=1}^M b_m \mathbf{p}_{o,m} \quad (8)$$

The weight  $b_m$  is computed using the Least Squares method, and is then truncated  $b_m \in [-\sqrt{3}\lambda_m, \sqrt{3}\lambda_m]$ . Examples are shown in Fig. 5(a)–(g) when the weight  $b_m$  of PDM is changed. The PDM of renal cortex ( $\Psi_o^\lambda, \Psi_i^\lambda$ ) is generated according to Eq. (7).

During in the process of mesh deformation, the PDM of renal cortex ( $\Psi_o^\lambda, \Psi_i^\lambda$ ) is also adapted to constrain the deformation of the outer layer mesh  $\Psi_o^\tau$ . The task can be accomplished by minimizing the sum of surface distances between  $\Psi_o^\tau$  and  $\Psi_o^\lambda$ ,  $\Psi_o^\tau$  and  $\Psi_t$ , which integrate and balance the shape prior and image boundary information. The function to minimize is defined as

$$D_{\text{surface}}(v) = \frac{1}{N_s} \left( \omega_1 d(\Psi_o^\tau(v), \Psi_o^\lambda(v)) + \omega_2 d(\Psi_o^\tau(v), \Psi_t(v)) + \omega_3 \sum_v 1/g(\Psi_i^\lambda(v)) \right) \quad (9)$$

where,  $n_s$  denotes a normalization parameter;  $\omega_1$ ,  $\omega_2$  and  $\omega_3$  are the weights balancing the shape prior and image boundary information;  $g$  is gradient magnitude of the smoothed image.

In this phase, the initial outer mesh  $\Psi_o^\tau$  of the renal cortex is adapted to the coarse boundary of the kidney in the thresholded image  $I_b$  by using the model adaptation algorithm. The process can be iteratively employed to search the desirable meshes of the renal cortex based on the previously adapted meshes of the renal cortex by model deformation and parametric adaptation successively. The objective function in Eq. (4) is then computed. The model adaptation algorithm is stopped when the distance difference  $\Delta D$  between two iterations is lower than a threshold value  $D_t$ . The whole process is illustrated in Fig. 5(j)–(l).

### 3.3. Non-uniform graph search

The initialized shapes are assumed to be close to the true boundaries. The graph search algorithm is used to determine the new position of the vertices in the initialized renal cortex ( $\Psi_o^r, \Psi_i^r$ ). Compared to the previous work by Li et al. (2012), herein a novel graph is constructed and a new cost function is formulated based on multi-scale boundary detection, allowing detection of the optimal surfaces of renal cortex.

As developed in the LOGISMOS framework by Li et al. (2006), Garvin et al. (2008), and Yin et al. (2010), optimal surface detection can be transformed into finding a minimum-cost closed set in a corresponding vertex-weighted graph using max-flow/min-cut algorithm (Boykov and Kolmogorov, 2004). Briefly, this involves two important tasks. First, a 3-D graph for each surface should be properly constructed corresponding to the original image, especially for those detected surfaces that do not coincide with the intersection of the z-axis. Second, a cost function should be formulated, since it measures the unlikelihood that each node in the graph belongs to a particular surface, and determines the set of feasible surfaces with the lowest cost. The two important tasks were done independently by Li et al. (2012), which may not lead to effective multiple surface detection. Therefore, the first step of the proposed approach is the computation of a multi-scale cost function and generation of a multi-scale sampling space for the test image. Then, a non-uniform graph is constructed to detect surfaces optimally.

#### 3.3.1. Multi-scale boundary detection

The multi-scale boundary function measures surface likeliness by evaluating boundary information in a scale-space approach. The gradient magnitude of the input image is used to compute the weight of the node in graph and uniformly-spaced sample the node may lead to false detection of the outer surface as shown in Fig. 6(a) and (d). In the Hessian scale space, using a too small scale for the computation of the boundary information may not detect weak boundaries like in the inner surface of the renal cortex as shown in Fig. 6(e). On the other hand, a large scale may result in false responses and undesired fusion of nearby strong boundaries (Fig. 6(b)). Furthermore, the Hessian matrix for a voxel in an image is computed by the convolution with multi-scale second order partial derivatives of 3D Gaussian functions (Li et al., 2012; Frangi et al., 1998) (shown in Fig. 6(b)), and boundary responses go away from the true boundaries of an object as the scale is increasing (shown in Fig. 6(b) and (e)). To address this problem, another scale-space by the first order partial derivatives is used to compute the boundary information, non-uniformly sample the node and define the boundary in the scale-space,

$$B(x, y, z) = \max_{\sigma_{\min} \leq \sigma_s \leq \sigma_{\max}} (\sigma_s^\gamma \|\nabla I_{\sigma_s}(x, y, z)\|), \quad (10)$$

where  $\sigma_s$  denotes the standard deviation of Gaussian functions, which are a discretized value between  $\sigma_{\min}$  and  $\sigma_{\max}$  using a linear scale,  $\|\cdot\|$  is the computation of gradient magnitude,  $\gamma$  is the scale adapted parameter,  $\nabla I_{\sigma_s}(x, y, z)$  is the computation of gradient based on the first order partial derivatives of Gaussian functions, i.e.,

$$\nabla I_{\sigma_s}(x, y, z) = \begin{cases} \nabla I_{\sigma_s}^x(x, y, z) = I(x, y, z) * G_{\sigma_s}^x(x, y, z) \\ \nabla I_{\sigma_s}^y(x, y, z) = I(x, y, z) * G_{\sigma_s}^y(x, y, z) \\ \nabla I_{\sigma_s}^z(x, y, z) = I(x, y, z) * G_{\sigma_s}^z(x, y, z) \end{cases} \quad (11)$$

where,  $*$  is the convolution operation;  $G_{\sigma_s}^x(x, y, z)$ ,  $G_{\sigma_s}^y(x, y, z)$  and  $G_{\sigma_s}^z(x, y, z)$  are the first order partial derivatives of Gaussian functions.

#### 3.3.2. Non-uniform graph construction

The multi-scale boundary responses are obtained by selecting the maximum response over the range of all scales (Eq. (10)). The scale at which the response is maximal is further used to estimate the sampling steps for subsequent graph construction as shown in Fig. 7(b). A weighted and directed graph  $\mathbb{G}$  is constructed in a narrowband around the initialized PDM ( $\Psi_o^r, \Psi_i^r$ ). Note that the graph  $\mathbb{G}$  corresponding to the outer or inner surface of the initialized renal cortex, respectively. As Fig. 7(a) illustrates, each node of a column in  $\mathbb{G}_o$  for the outer surface or  $\mathbb{G}_i$  for the inner surface is sampled along the gradient direction in Euclidean distance field of an initial kidney  $\Psi_o^r$ . This procedure is designed in an adaptive fashion to detect optimal surface and avoid incorrect local surface propagation (Li et al., 2012). The sampling steps for the  $k$ th vertex  $\mathbf{v}_k$  on the outer or inner surface are computed along the gradient direction  $\mathbf{g}_k(\mathbf{p}_k^i)$  by using the distance to the desirable surface: the smaller step size for the neighboring region of the desirable surface while the larger step size for the regions far from the desirable surface. To address this, the intra-column sampling step is computed by

$$d_k^{\text{intra}}(\mathbf{p}_k) = f_d(B(\mathbf{p}_k)), \quad (12)$$

where  $\mathbf{p}_k$  indicates the coordinate of the  $k$ th vertex on the outer or inner surface along the gradient direction  $\mathbf{g}_k(\mathbf{p}_k^i)$  (or the opposite direction  $-\mathbf{g}_k(\mathbf{p}_k^i)$ ), and  $f_d$  is a linear function mapping boundary information into a step size, i.e., high value to small step size and vice versa. Once the sampled points are obtained to generate the columns, the cost can be computed for each node in the graph  $\mathbb{G}$ . Computation of coordinates is heavy; therefore, herein coordinates for each sampled point are recursively computed from the initialized mesh of the outer surface as

$$\mathbf{p}_k = \begin{cases} \mathbf{p}_k^i = \mathbf{p}_k^{i-1} + d_k^{\text{intra}}(\mathbf{p}_k^{i-1}) \cdot \mathbf{g}_k(\mathbf{p}_k^{i-1}) & 1 \leq i \leq N_u; \\ \quad \cdot d_k^{\text{intra}}(\mathbf{p}_k^{i-1}), & \\ \mathbf{p}_k^j = \mathbf{p}_k^{j-1} - d_k^{\text{intra}}(\mathbf{p}_k^{j-1}) \cdot \mathbf{g}_k(\mathbf{p}_k^{j-1}) & 1 \leq j \leq N_b; \\ \quad \cdot d_k^{\text{intra}}(\mathbf{p}_k^{j-1}), & \\ \mathbf{p}_k^i = \mathbf{p}_k^j = \mathbf{v}_k = (x_k, y_k, z_k), & i = j = 0. \end{cases} \quad (13)$$

where  $\mathbf{p}_k^i$  is coordinate of the  $i$ th sampled point along the gradient direction  $\mathbf{g}_k(\mathbf{p}_k^{i-1})$  ( $i = 1, \dots, N_u$ ),  $\mathbf{p}_k^j$  is coordinate of the  $j$ th sampled point along the gradient direction  $\mathbf{g}_k(\mathbf{p}_k^{j-1})$  ( $j = 1, \dots, N_b$ ), and  $N_u$  and  $N_b$  are the number of sampled points along and opposite the normal direction, respectively.

After all nodes are obtained for the outer or inner surface, nodes in graph  $\mathbb{G}$  can be connected with three types of weighted and directed arcs: the intra-column arc  $E^{\text{intra}}$ , the inter-column arc  $E^{\text{inter}}$ , and the terminal arc  $E^{\text{terminal}}$ . The intra-column arc  $E^{\text{intra}}$  connects two neighboring nodes in a column from up to bottom as shown in Fig. 7(b) (the green arrows). The inter-column arc  $E^{\text{inter}}$  connects two neighboring nodes in two neighboring columns from up to bottom as shown in Fig. 7(b) (the black arrows). The terminal arc  $E^{\text{terminal}}$  connects all nodes in  $\mathbb{G}$  to two terminal nodes  $S$  or  $T$ , if the weight is positive then the node is connected to the terminal node  $S$ ; otherwise, the node is connected to the terminal node  $T$ . For the  $k$ th column in a graph, a node can be denoted as  $V_k^{l_v}$  for the graph  $\mathbb{G}$  ( $l_v = 1, 2, \dots, N_u + N_b + 1$ ). The node in the neighboring  $k'$ th column can be denoted as  $V_{k'}^{l_v}$ . Mathematically, the three types of arcs can be written as,

$$E^{\text{intra}} = \langle V_k^{l_v}, V_k^{l_v-1} \rangle, \quad (14)$$

$$E^{\text{inter}} = \langle V_k^{l_v}, V_{k'}^{l_v-\mu} \rangle, \quad (15)$$

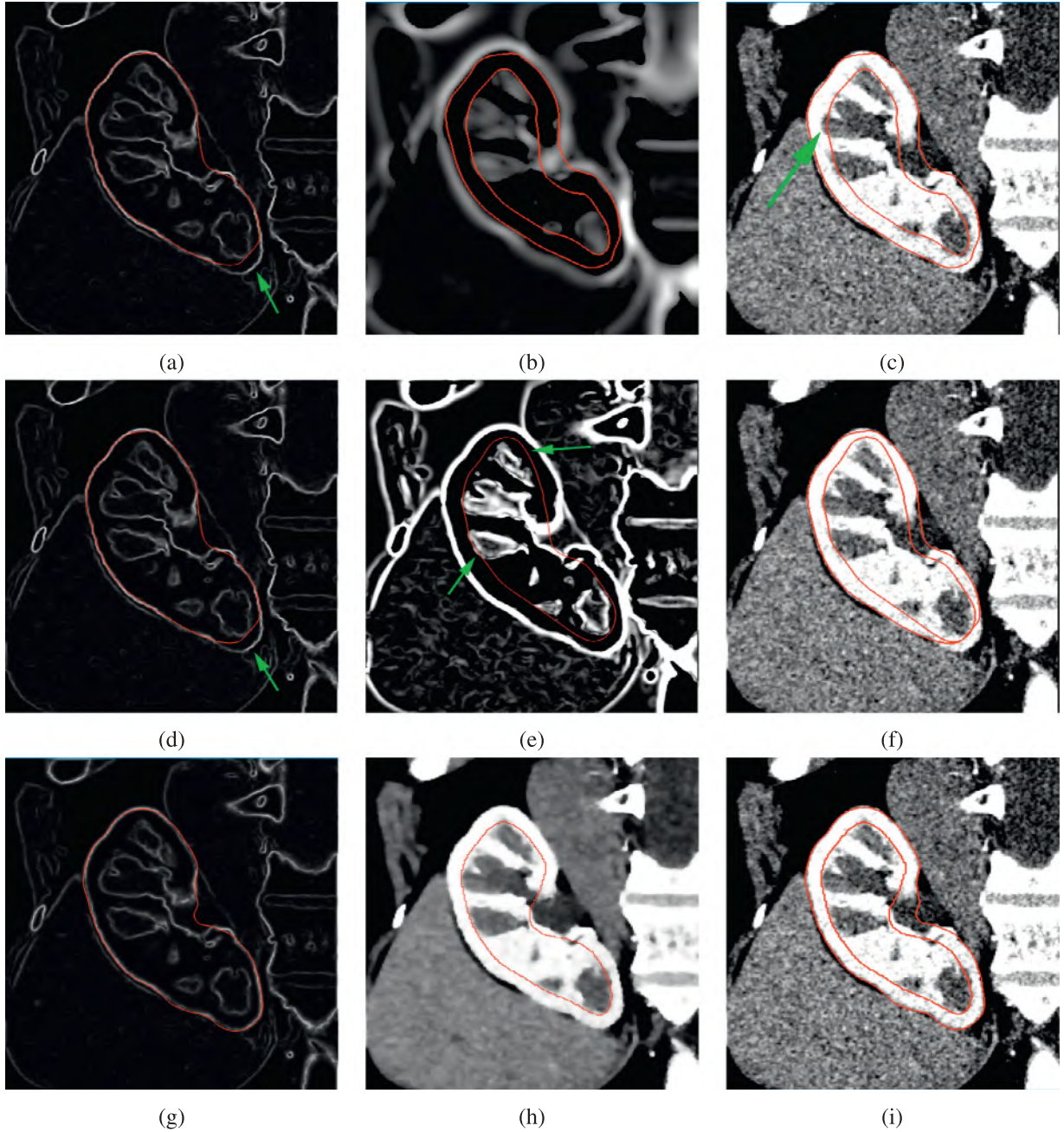


**Fig. 6.** Boundary computation in multi-scale space. (a) The gradient magnitude image is used as the cost image for the refinement of the outer surface (the red curve); (b) Hessian-based image ( $\sigma_s = 3.0$ ) is used as the cost image for the refinement of the inner surface (the red curve); (c) The original image, the refined outer and inner surfaces (the red curves) using the method proposed by Li et al. (2012); (d) The gradient magnitude image is used as the cost image for the refinement of the outer surface (the red curve), and graph search is applied iteratively; (e) Hessian-based image ( $\sigma_s = 1.0$ ) is used as the cost image for the refinement of the inner surface (the red curve); (f) The original image and the refined outer and inner surfaces (the red curves) using the method proposed by Li et al. (2012); (g) The boundary responses in multiple scale space by the first order partial derivatives is used as the cost image for the refinement of the outer surface by using the proposed non-uniform graph search (the red curve); (h) The filtered image is used as the cost image for the refinement of the inner surface (the red curve) by using the proposed non-uniform graph search (the red curve); (i) The original image, the refined outer and inner surfaces (the red curves) using by using the proposed non-uniform graph search (the red curves). (For interpretation of the references to colour in this figure legend, the reader is referred to the web version of this article.)

$$E^{terminal} = \begin{cases} \langle S, V_k^{l_v} \rangle, & \omega(V_k^{l_v}) > 0; \\ \langle V_k^{l_v}, T \rangle, & \omega(V_k^{l_v}) \leq 0; \end{cases} \quad (16)$$

where  $\mu$  is the inter-column smoothness constraint for the outer or inner surface.  $\omega$  is the weight of a node  $V_k^{l_v}$ . For the first two types of arcs  $E^{intra}$  and  $E^{inter}$ , the cost is set to infinity. The cost of terminal arcs can be defined as the absolute value of the weight of the corresponding node. The weight of a node for the outer or

inner surface is defined as

$$\begin{cases} \omega(V_{ok}^{l_v}) = -B(p_{ok}^{l_v}) + B(p_{ok}^{l_v-1}), & l_v = 2, 3, \dots, \\ \omega(V_{ok}^{l_v}) = -B(p_{ok}^{l_v}), & N_u + N_b + 1; \\ \omega(V_{ik}^{l_v}) = -I(p_{ik}^{l_v}) + I(p_{ik}^{l_v-1}), & l_v = 1; \\ \omega(V_{ik}^{l_v}) = -I(p_{ik}^{l_v}), & l_v = 2, 3, \dots, \\ & N_u + N_b + 1; \\ & l_v = 1, \end{cases} \quad (17)$$

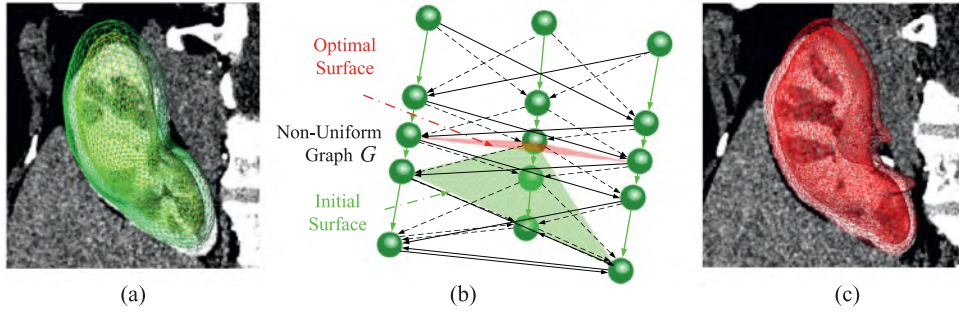


**Fig. 7.** Graph Construction. (a) The initialized outer and inner surfaces; (b) The proposed non-uniform graph for optimal surface detection; (c) The refined outer and inner surfaces by using the proposed non-uniform graph for optimal surface detection.

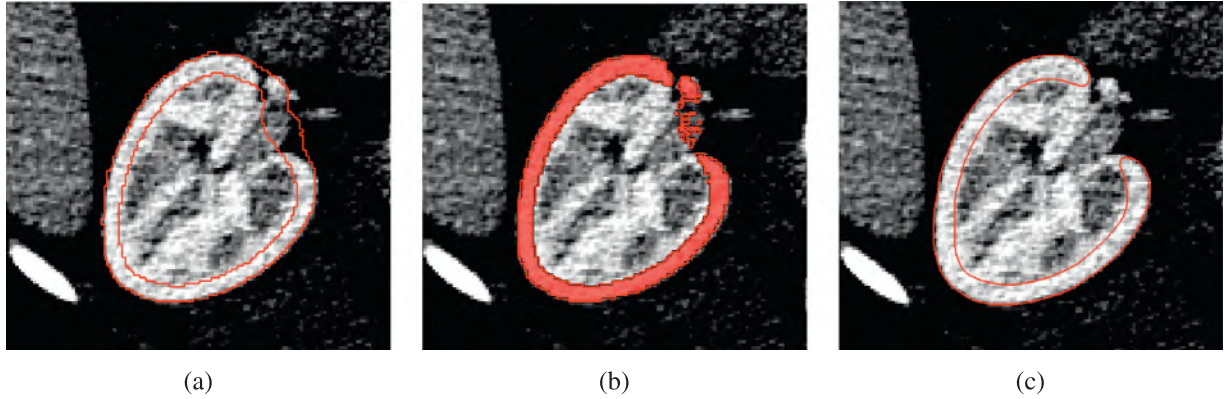


**Fig. 8.** Final renal cortex generation. (a) The binary images of the outer and inner surfaces; (b) The coarse renal cortex; (c) The refined renal cortex.

where,  $\omega(V_{ok}^{lv})$  is the weight of the node in the graph  $\mathbb{G}_o$  for the outer surface,  $B(\mathbf{p}_{ok}^{lv})$  is the boundary information in multi-scale space for the node  $V_{ok}^{lv}$  in the graph  $\mathbb{G}_o$  for the outer surface,  $\mathbf{p}_{ok}^{lv}$  computed by Eq. (13) is the coordinate of the node  $V_{ok}^{lv}$  in the boundary image;  $\omega(V_{ik}^{lv})$  is the weight of the node in the graph  $\mathbb{G}_i$  for the inner surface,  $I(\mathbf{p}_{ik}^{lv})$  is the filtered image intensity for the node  $V_{ik}^{lv}$  in the graph  $\mathbb{G}_i$  for the inner surface,  $\mathbf{p}_{ik}^{lv}$  is also the coordinate of the node  $V_{ik}^{lv}$  in the boundary image and computed as Eq. (13). There are two reasons why the weights of nodes for the inner surface is computed according to the filtered image intensity. First, the second order partial derivatives of images may lead to boundary deviation as illustrated in Fig. 6; second, the inner boundary is much weaker than the outer boundary, and the first order partial derivative is small, the under-segmentation or over-segmentation of the inner surface may result. The outer and inner surfaces are converted into binary images as shown in Fig. 8(a). The coarse renal cortex is then obtained by subtracting the inner binary image from the outer binary image. A simple thresholding method is applied to the filtered image combined with the coarse renal cortex as shown in Fig. 8(b). For each slice in axial view as shown in Fig. 8(b), the run length encoding method (Ibanez et al., 2005) is used to label the connected components and represent the binary objects. The connected component with the largest number of pixels is kept in the binary label image in order to remove small regions such as renal arteries and renal veins as shown in Fig. 8(c).

#### 4. Parameter selection for reproducible research

##### 1) Renal Cortex Model Construction

In creating statistical shape of renal cortex, the kidneys and closed inner regions including medulla and pelvis were manually

traced for each original volume. The binary volume of kidneys and closed inner regions were subsequently transformed into outer surfaces and inner surfaces, respectively. The two types of surfaces were simplified as triangle meshes with 3000 vertices. After obtaining the corresponding relationship and parameters of similarity transformation, the amount of shape variance of outer and inner surfaces were truncated at 98% of the total variation present in the training set.

##### 2) Renal Cortex Initialization

The variance of the Gaussian smoothing filter was set to 1, and its kernel width was set to 9. The corresponding angle steps  $t_\alpha$  and  $t_\beta$  were both set to  $9^\circ$ . A threshold value  $b = 0.4$  was used to obtain a rough contour of the kidney. A morphological opening with spherical structuring elements (radius was set to 2) was used to remove small structures.  $\kappa = 25$  typically can control the balance between region and surface constraints. In our experiments, the voxel spacing range is 0.5 mm to 5.0 mm;  $n_t = 5$  were appropriate to efficiently deform the initial surface. For the consideration of memory usage, the number of sampling points  $n_m$  was set to 20. The bounding box is computed for the outer layer mesh and is broadened with 20 voxels in the six end points so as to obtain a local binary image and compute the signed Euclidean distance fields. In the implementation of renal cortex model adaptation, the mean shape model of renal cortex was adapted in the eigen-space with the truncation between  $-\sqrt{3\tilde{\lambda}_m}$  to  $\sqrt{3\tilde{\lambda}_m}$  of the eigenvalues computed by PCA. Renal cortex initialization is stopped as the distance difference  $\Delta D$  is lower than the threshold value  $D_t = 0.01$ .

##### 3) Renal Cortex Segmentation

After obtaining the initial renal cortex, a local rectangular region extending the bounding box by 50 pixels was used to detect the outer and inner surface. The local image was linearly interpolated higher resolutions with voxel spacings  $0.25 \text{ mm} \times 0.25 \text{ mm} \times 0.25 \text{ mm}$ . In this study, we used the curvature anisotropic

diffusion filtering (Whitaker and Xue, 2001), which enhances the renal cortex boundaries while minimizing the noise. When smoothing by this filter, the conductance parameter  $\lambda_a$  was set to 3, the time step  $t_a$  was 0.06, the number of iterations  $n_a$  was typically set to 10. In terms of computing the multi-scale boundary, the scales  $\sigma_s$  were set as 1.0, 1.5 and 2.0, respectively, and the scale adapted parameter  $\gamma = 0.6$ . Based on the minimal and the maximal scales, the intra-column sampling step  $d_{ok}^{\text{intra}}(\mathbf{p}_{ok})$  was linearly mapped to [0.01 mm, 0.6 mm] and  $d_{ik}^{\text{intra}}(\mathbf{p}_{ik})$  was linearly mapped to [0.1 mm, 0.5 mm] according to Eq. (12). The number of sampled points  $N_u$  and  $N_b$  was 15. The smoothness constraint  $\mu$  was set to 1.

## 5. Experiments

### 5.1. Subject data

The proposed method was tested on a clinical CT data set consisting of 58 abdominal volume datasets acquired during pre-operative screening and containing contrast-enhanced images acquired from two different types of CT scanners (GE Medical systems, LightSpeed Ultra; and Philips, Mx8000 IDT 16). The pixel size varied from 0.63 to 1 mm, slice thickness from 0.5 to 5 mm and slice numbers from 54 to 525. The reference delineation was provided by experienced experts.

### 5.2. Evaluation metrics and comparisons

Eight surface- and volume-based segmentation metrics were used to evaluate the results of the proposed approach (Heimann et al., 2009; Li et al., 2012): Average Symmetric Surface Distance (in mm) (ASSD), Average Symmetric Root Mean Square Surface Distance (in mm) (ASRMSSD), Signed Relative Volume Difference (%) (SRVD), Volume Overlap Error (%) (VOE), True Positive Fraction (%) (TPF), False Positive Fraction (%) (FPF), and Dice Similarity Coefficient (%) (DSC). Paired t-tests were used to compare the segmentation errors in DSC and a  $p$ -value less than 0.05 was considered statistically significant.

To quantitatively evaluate the performance of our method, we compared the segmentation results to previously established methods: the graph cut based method (Chen et al., 2012a), Traditional Graph Search method (TGS), Iterative Traditional Graph Search method (ITGS), the Hessian based graph search method (Li et al., 2012), the random forest based method (Jin et al., 2016), and our proposed Non-Uniform Graph Search (NUGS). We used the cross-validation evaluation strategy, one data set consists of 36 CT scans and the other contains 22 CT scans. Two renal cortex shape models were trained for cross-initialization for TGS and NUGS, and two random forest classifiers were also trained for renal cortex segmentation for the random forest based method. Our method was implemented in C++ and tested on a 64-bit desktop PC (3.1 GHz Core (TM) i5-3450 CPU and 16 GB RAM).

### 5.3. Experimental results

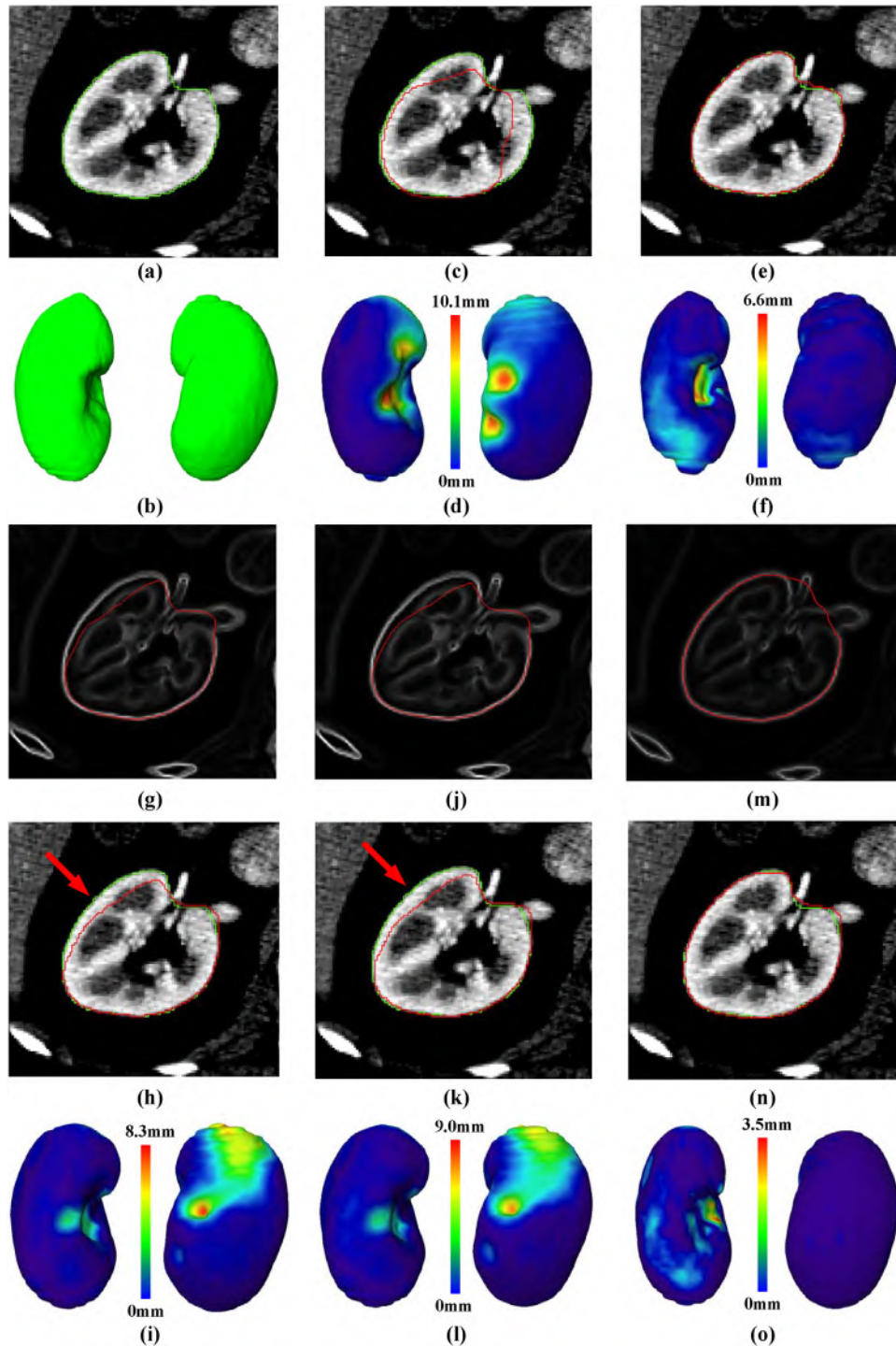
#### 5.3.1. Kidney segmentation

We compared our approach with the closely related methods: Chen et al. (2012a), Jin et al. (2016), TGS, ITGS and Li et al. (2012). To make a fair comparison to the most closely related method: TGS and ITGS, the same kidney segmentation framework is used in these graph search based methods, i.e., the same shape correspondence establishment, shape initialization strategy and post-processing. The only difference is the graph search optimization method used to refine the kidney surface. In TGS and ITGS, the weight of the node was computed according to the gradient magnitude of the filtered images to compute the weights of nodes and detect the final outer surface.

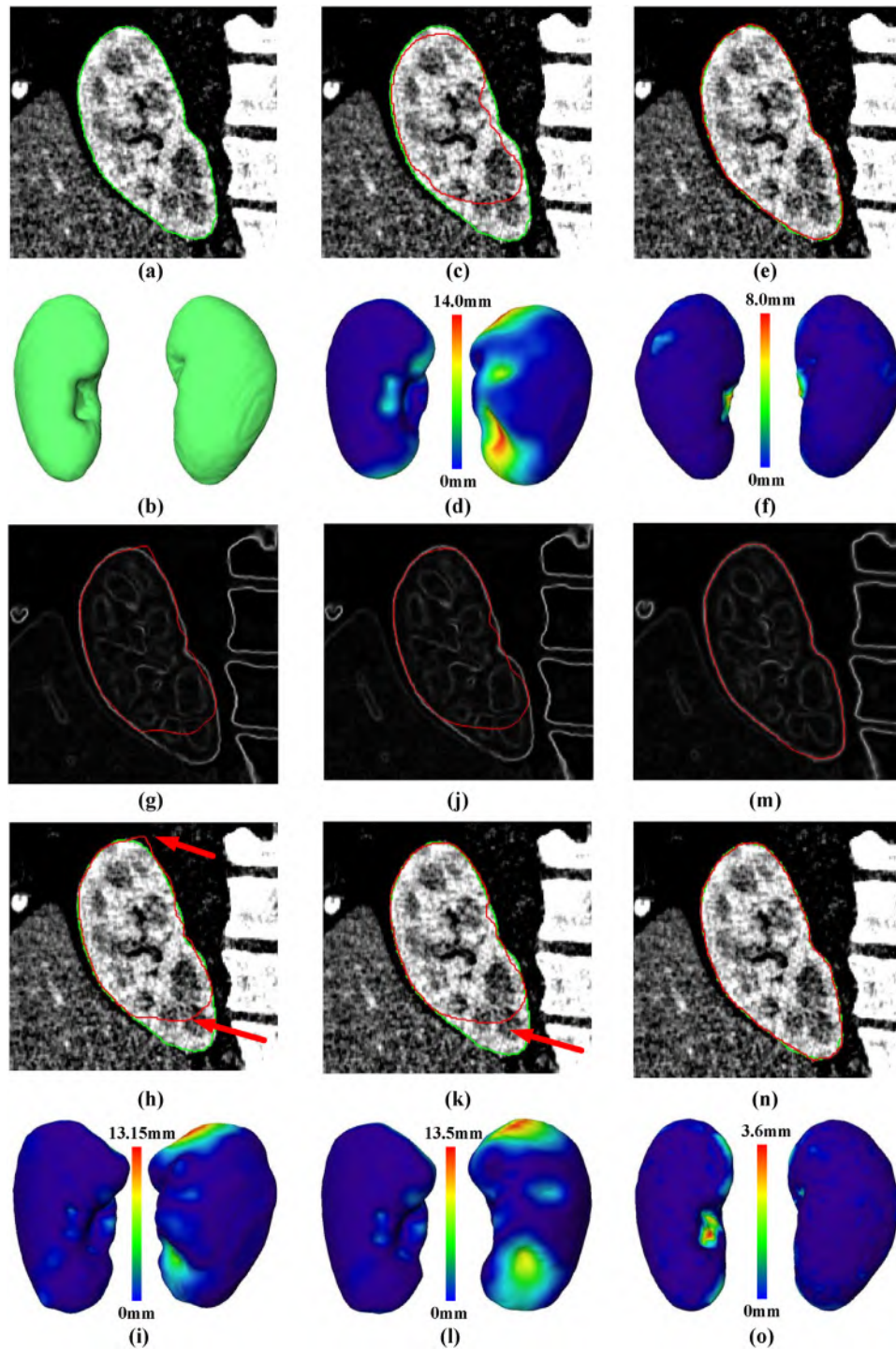
Fig. 9 compares one kidney segmentation case between initialization, the random forest based method (Jin et al., 2016), TGS, ITGS and our NUGS method in a challenging case where the contrast between renal cortex and renal medulla is the similar as that between renal cortex and background. One original image slice was shown in Fig. 9(a). The 3D visualization of reference segmentation in two view points was shown in Fig. 9(b). As can be seen in Fig. 9(c), the initial outer surface was coarsely detected by using the model adaptation procedure; however, one part of the surface stopped at the boundary between renal cortex and renal medulla since the intensity value is very low and close to the background near the liver. Thus, surface distance between the initialized outer surface and reference segmentation achieved to 10.1mm as shown in Fig. 9(d). Fig. 9(g) shows the gradient magnitude image was used to compute the weight of the node for TGS, and the detected outer surface still stopped at the boundary between renal cortex and renal medulla. Even though the ITGS method was employed, the detected outer surface did not still moved to the outer boundary of the kidney as shown in Fig. 9(j)–(k). As can be seen in Fig. 9(m)–(n), the multi-scale boundary image was used to compute the weight of the node and the proposed non-uniform graph search method successfully made the initial outer surface move to the outer boundary of the kidney. By contrast, surface distance was much smaller between the outer surface by using the proposed non-uniform graph search method and reference segmentation as shown in Fig. 9(o).

Fig. 10 compares one kidney segmentation case between initialization, the random forest based method (Jin et al., 2016), TGS, ITGS and our NUGS method in a challenging case where one pole of the kidney is slender. One original image slice in coronal view was shown in Fig. 10(a). The 3D visualization of reference segmentation in two view points was shown in Fig. 10(b). In the model adaptation step, the initial outer surface was far from the pole of the kidney as shown in Fig. 10(c). The reason is that in model adaptation process, there was a large renal medulla loculus and morphological operations can not fill this region. Similarly in both TGS method and ITGS method, the detected outer surface did not still moved to the outer boundary of the kidney as shown in Fig. 10(g)–(i). The TGS methods tended to produce under-segmentation as pointed by Li et al. (2012). By contrast, in our method these under-segmented regions were effectively extracted as shown in Fig. 10(n). These experimental results demonstrated the robustness of our method against under-segmentation of the kidney.

Segmentation evaluation is shown in Table 1. As can be seen in the 1st and 2nd columns of Table 1, distances between the detected outer surface and the reference kidney segmentation were  $0.41 \pm 0.51$  mm in ASSD and  $1.04 \pm 1.00$  mm in ASRMSSD, which were slightly larger than the results reported by Li et al. (2012). In the paper of Li et al. (2012), authors used only 17 CT images to test their method. In the 3rd column of Table 1, volume difference SRVD was negative and much smaller than zero in the initialization step ( $-16.09 \pm 10.52\%$ ), TGS method ( $-10.09 \pm 8.55\%$ ), random forest based method ( $-11.17 \pm 6.91\%$ ) and ITGS method ( $-9.18 \pm 8.10\%$ ). This measure showed that these methods produce under-segmentation of the kidneys. Specially, performance of the ITGS method was slightly improved compared to that of TGS (Paired t-tests in DSC,  $p = 6.97 \times 10^{-4}$ ). In the paper of Chen et al. (2012a), authors used a voxel labeling method, an iterative shape-constrained graph cut, to segment the kidney. The TPF and FPF for the kidney segmentation were  $96.32 \pm 6.12\%$  and  $0.29 \pm 0.05\%$ , respectively. The FPF was larger than the other method. The TPF was smaller than the proposed NUGS method. The DSC was  $97.86 \pm 2.41\%$ , which showed the proposed NUGS method outperformed (Li et al., 2012).



**Fig. 9.** Kidney segmentation (the green curve is reference segmentation and the red curve is the detected kidney). (a) The original image in axial view; (b) The 3D visualization of reference segmentation; (c) The initialized outer surface; (d) The 3D visualization of surface distance between the initialized outer surface and reference segmentation; (e) The outer surface by using the random forest based method (Jin et al., 2016); (f) The 3D visualization of surface distance between the outer surface by using the random forest based method (Jin et al., 2016) and reference segmentation; (g) The gradient magnitude image and the detected outer surface by using traditional graph search method; (h) The original image and the detected outer surface by using traditional graph search method; (i) The 3D visualization of surface distance between the outer surface by using traditional graph search method and reference segmentation; (j) The gradient magnitude image and the detected outer surface by using iterative traditional graph search method; (k) The original image and the detected outer surface by using traditional iterative graph search method; (l) The 3D visualization of surface distance between the outer surface by using traditional iterative graph search method and reference segmentation; (m) The multi-scale boundary image and the detected outer surface by using the proposed non-uniform graph search method; (n) The original image and the detected outer surface by using the proposed non-uniform graph search method; (o) The 3D visualization of surface distance between the outer surface by using the proposed non-uniform graph search method and reference segmentation. (For interpretation of the references to colour in this figure legend, the reader is referred to the web version of this article.)



**Fig. 10.** Kidney segmentation (the green curve is reference segmentation and the red curve is the detected kidney). (a) The original image in coronal view; (b) The 3D visualization of reference segmentation; (c) The initialized outer surface; (d) The 3D visualization of surface distance between the initialized outer surface and reference segmentation; (e) The outer surface by using the random forest based method (Jin et al., 2016); (f) The 3D visualization of surface distance between the outer surface by using the random forest based method (Jin et al., 2016) and reference segmentation; (g) The gradient magnitude image and the detected outer surface by using traditional graph search method; (h) The original image and the detected outer surface by using traditional graph search method; (i) The 3D visualization of surface distance between the outer surface by using traditional graph search method and reference segmentation; (j) The gradient magnitude image and the detected outer surface by using traditional iterative graph search method; (k) The original image and the detected outer surface by using traditional iterative graph search method; (l) The 3D visualization of surface distance between the outer surface by using traditional iterative graph search method and reference segmentation; (m) The multi-scale boundary image and the detected outer surface by using the proposed non-uniform graph search method; (n) The original image and the detected outer surface by using the proposed non-uniform graph search method; (o) The 3D visualization of surface distance between the outer surface by using the proposed non-uniform graph search method and reference segmentation. (For interpretation of the references to colour in this figure legend, the reader is referred to the web version of this article.)

**Table 1**

Quantitative results and comparative performance evaluation for kidney segmentation (mean standard deviation). The bold numbers identify the best results.

Method	ASSD[mm]	ASRMSSD[mm]	SRVD[%]	VOE[%]	TPF[%]	FPF[%]	DSC[%]
Initialization	2.01 ± 1.35	2.99 ± 1.99	-16.09 ± 10.52	18.92 ± 8.87	82.32 ± 9.08	0.01 ± 0.03	89.26 ± 5.96
TGS	1.43 ± 1.08	2.51 ± 1.72	-10.09 ± 8.55	13.66 ± 7.30	87.97 ± 7.39	0.01 ± 0.03	92.49 ± 4.60
Jin et al.	1.28 ± 0.87	2.20 ± 1.50	-11.17 ± 6.91	13.27 ± 6.32	87.71 ± 6.55	0.01 ± 0.01	92.77 ± 3.81
ITGS	1.35 ± 1.00	2.37 ± 1.67	-9.18 ± 8.10	13.16 ± 6.69	88.67 ± 6.82	0.01 ± 0.03	92.80 ± 4.16
Chen et al.	/	/	/	/	96.32 ± 6.12	0.29 ± 0.05	
Li et al.	<b>0.14 ± 0.09</b>	<b>0.66 ± 0.61</b>	1.42 ± 2.44	<b>2.43 ± 2.22</b>	/	/	96.55 ± 1.77
NUGS	0.41 ± 0.51	1.04 ± 1.00	<b>1.23 ± 5.29</b>	4.09 ± 4.41	<b>98.44 ± 2.84</b>	<b>0.02 ± 0.03</b>	<b>97.86 ± 2.41</b>

### 5.3.2. Renal cortex segmentation

The single scale Hessian based cost function ( $\sigma_s = 1.0, 3.0$ ) was used to detect the inner surface for IGS method. In our experiments, the inner surface was detected by graph search methods from the same initialized surfaces so as to compare the performance of these methods.

Fig. 11 compares one renal cortex segmentation case (the same image as in Fig. 9) between initialization, the random forest based method (Jin et al., 2016), Hessian-based ( $\sigma_s = 3.0$ ) TGS, Hessian-based ( $\sigma_s = 1.0$ ) TGS and our NUGS method. Fig. 11(a) shows the original image in axial view. Fig. 11(b) shows the 3D visualization of reference segmentation. The initialized renal cortex was under-segmented as shown in Fig. 11(c). However, the random forest based method tended to produce over-segmentation as shown in Fig. 11(e) since thickness and intensity range of the renal column was similar as those of the renal cortex. Surface distance between the inner surface and reference annotation was mostly large as shown in Fig. 11(f). Fig. 11(g) shows the Hessian-based image ( $\sigma_s = 3.0$ ) and the inner surface was detected by using traditional graph search method. The inner surface stopped at the boundary of the sheet structures computed according to a single scale second order partial derivative (also Hessian matrix based); however, the boundary was far from the true boundary between renal cortex and renal medulla as shown in Fig. 11(h). Due to the under-segmentation of the kidney in this case, renal cortex was under-segmented as shown in Fig. 11(i). The inner surface was much closer for the smaller scale ( $\sigma_s = 1.0$ ) as shown in Fig. 11(j); however, renal cortex was also under-segmented as shown in Fig. 11(k)–(l). Fig. 11(m) shows the filtered image was used for the proposed non-uniform graph search method to successfully detect the inner surface.

Fig. 12 compares one renal cortex segmentation case (the same image as Fig. 10) between initialization, the random forest based method (Jin et al., 2016), Hessian-based ( $\sigma_s = 3.0$ ) TGS, Hessian-based ( $\sigma_s = 1.0$ ) TGS and our NUGS method. Fig. 12(a) shows the original image in coronal view. Fig. 12(b) shows the 3D visualization of reference segmentation. As can be seen in Fig. 12(c)–(d), initial renal cortex was falsely detected at the pole of the kidney due to the under-segmentation of the kidney. The random forest based method tended to produce over-segmentation of renal cortex and contain renal column and rib as shown in Fig. 12(e)–(f). Surface distance between the inner surface and reference annotation was also mostly large as shown in Fig. 12(f). The Hessian-based methods for both  $\sigma_s = 3.0$  and  $\sigma_s = 1.0$  produced severe under-segmentation of renal cortex as shown in Fig. 11(g)–(l). As can be seen in Fig. 12(n)–(o), renal cortex was accurately segmented except for a few structures.

Segmentation evaluation for renal cortex is shown in Table 2. As can be depicted in the 1st and 2nd column of Table 2, surface distances between the detected renal cortex to the reference renal cortex segmentation were  $0.12 \pm 0.17$  mm in ASSD and  $0.61 \pm 0.44$  mm in ASRMSSD. The overall surface distance illustrated that the proposed NUGS outperformed the other methods. SRVD was  $-13.01 \pm 15.33\%$ . It means the inner and outer surfaces

initially produced under-segmentation using the proposed model adaptation method. SRVD was  $15.68 \pm 22.47\%$  for the Hessian-based method ( $\sigma_s = 3.0$ ), and SRVD was  $33.31 \pm 15.52\%$  for the random forest based method (Jin et al., 2016). It means these two methods produced over-segmentation on the whole. Compared to the Hessian-based method with a larger single scale second order partial derivative, renal cortex segmentation performance was improved to the Hessian-based method with a smaller single scale second order partial derivative as can be seen in the 2nd row and the 4th row of Table 2 (Paired t-tests in DSC,  $p = 3.51 \times 10^{-11}$ ). The TPF and FPF for the renal cortex segmentation by using iterative shape-constrained graph cut (Chen et al., 2012a) were  $90.15 \pm 3.11\%$  and  $0.85 \pm 0.05\%$ , respectively. By contrast, the TPF and FPF for the renal cortex segmentation by using NUGS were  $98.71 \pm 3.47\%$  and  $0.01 \pm 0.01\%$ , respectively. The overall DSC of NUGS was  $97.48 \pm 3.18\%$ .  $p$  values were  $1.32 \times 10^{-32}$  (NUGS vs the Hessian-based method ( $\sigma_s = 3.0$ )),  $1.80 \times 10^{-25}$  (NUGS vs the Hessian-based method ( $\sigma_s = 1.0$ )),  $1.31 \times 10^{-28}$  (NUGS vs the random forest based method) in paired t-tests. The total running time of the proposed approach was approximately 5 minutes.

## 6. Conclusion and future work

In this paper, we present a novel framework, named *CortexExpert*, that improves the performance of the renal cortex quantification. The proposed method was tested on 58 clinical CT images. An overall segmentation accuracy of  $97.86\% \pm 2.41\%$  and  $97.48\% \pm 3.18\%$  for kidney and cortex segmentation, respectively. First, the statistical shape model of the renal cortex is established so that we can automatically initialize the outer surface and the inner surface of the renal cortex in a test image. Second, renal cortex initialization can provide approximate inner and outer surfaces of the kidney and make it much easier to detect the weak boundary of the inner layer and remove the renal column. Third, we introduce a non-uniform graph search algorithm to detect the optimal boundary of the renal cortex. Compared to the traditional multi-surface graph search method, a new cost function is formulated based on multi-scale boundary detection and a non-uniform graph is constructed. Nodes are non-equidistantly sampled according to the initial surface. Sample points are denser in the regional candidate boundaries while they are sparser further from candidate boundaries. The presented graph search algorithm can improve accuracy for renal cortex segmentation since we can control sampling steps.

Despite all significant improvements in renal cortex segmentation, several limitations of the proposed segmentation method exist. Renal cortex segmentation may still be imperfect in certain cases where anatomical and pathology induced variations are not captured by the model. As can be seen in Fig. 13, kidney anatomy in this example is unexpectedly different: Fig. 13(a)–(b) shows  $180^\circ$  rotation with respect to the conventional positioning of the normal kidneys. Moreover, part of the renal cortex is missing. Renal veins and arteries are highly enhanced with contrast agent such that the boundaries between the renal cortex and renal veins and/or arteries are not clear, contributing to segmentation errors. One may

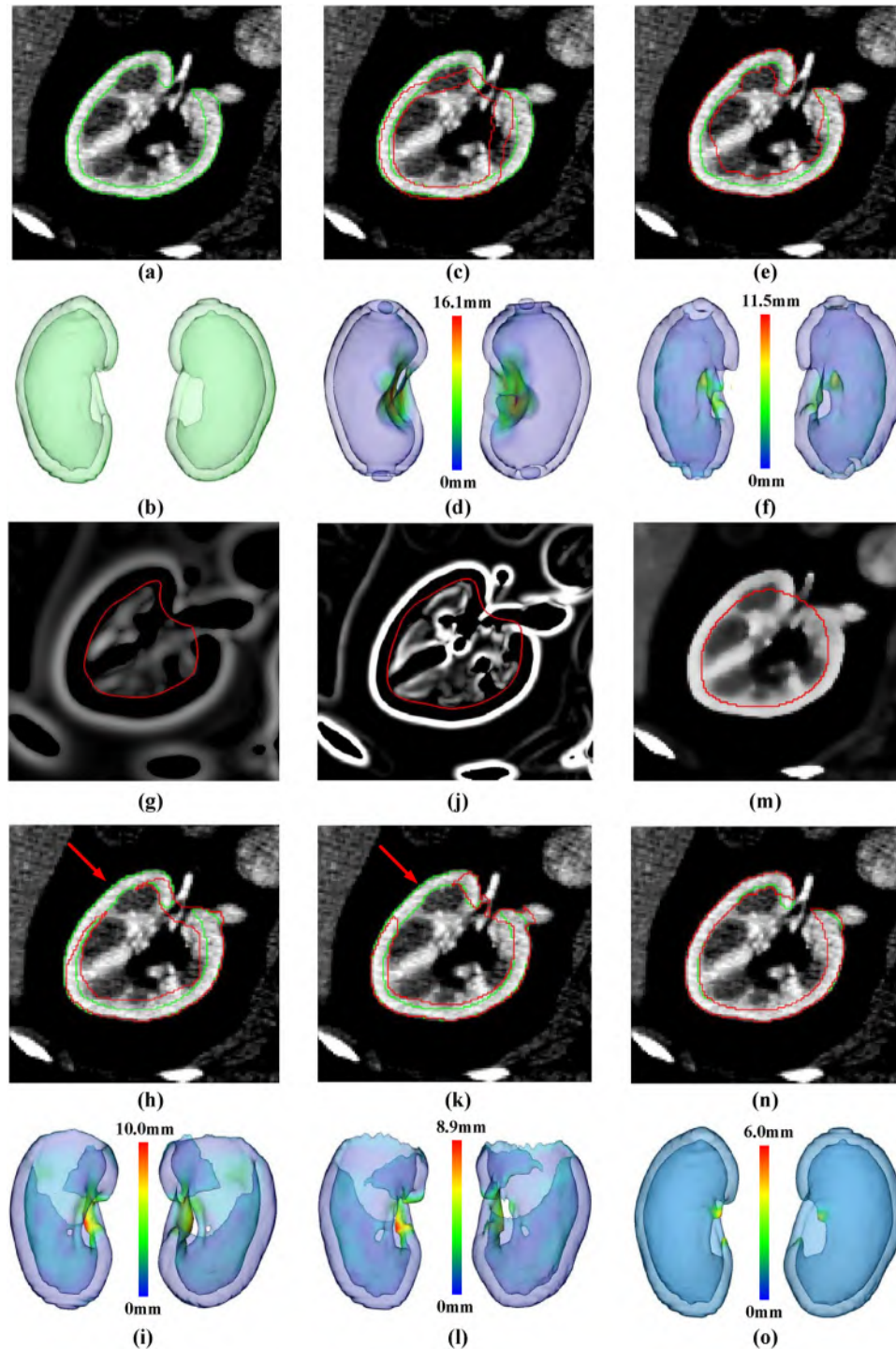


**Fig. 11.** Renal cortex segmentation (the green curve is reference segmentation and the red curve is the detected surface). (a) The original image in axial view; (b) The 3D visualization of reference segmentation; (c) The initialized renal cortex; (d) The 3D visualization of surface distance between the initialized renal cortex and reference segmentation; (e) The renal cortex by using the random forest based method (Jin et al., 2016); (f) The 3D visualization of surface distance between the detected renal cortex by using the random forest based method (Jin et al., 2016) and reference segmentation; (g) The Hessian-based image ( $\sigma_s = 3.0$ ) and the inner surface by using traditional graph search method; (h) The original image and the detected renal cortex by using traditional graph search method; (i) The 3D visualization of surface distance between the detected renal cortex by using traditional graph search method and reference segmentation; (j) The Hessian-based image ( $\sigma_s = 1.0$ ) and the detected inner surface by using traditional graph search method; (k) The original image and the detected renal cortex by using traditional graph search method; (l) The 3D visualization of surface distance between the renal cortex by using traditional graph search method and reference segmentation; (m) The filtered image and the detected inner surface by using the proposed non-uniform graph search method; (n) The original image and the detected renal cortex by using the proposed non-uniform graph search method; (o) The 3D visualization of surface distance between the renal cortex by using the proposed non-uniform graph search method and reference segmentation. (For interpretation of the references to colour in this figure legend, the reader is referred to the web version of this article.)

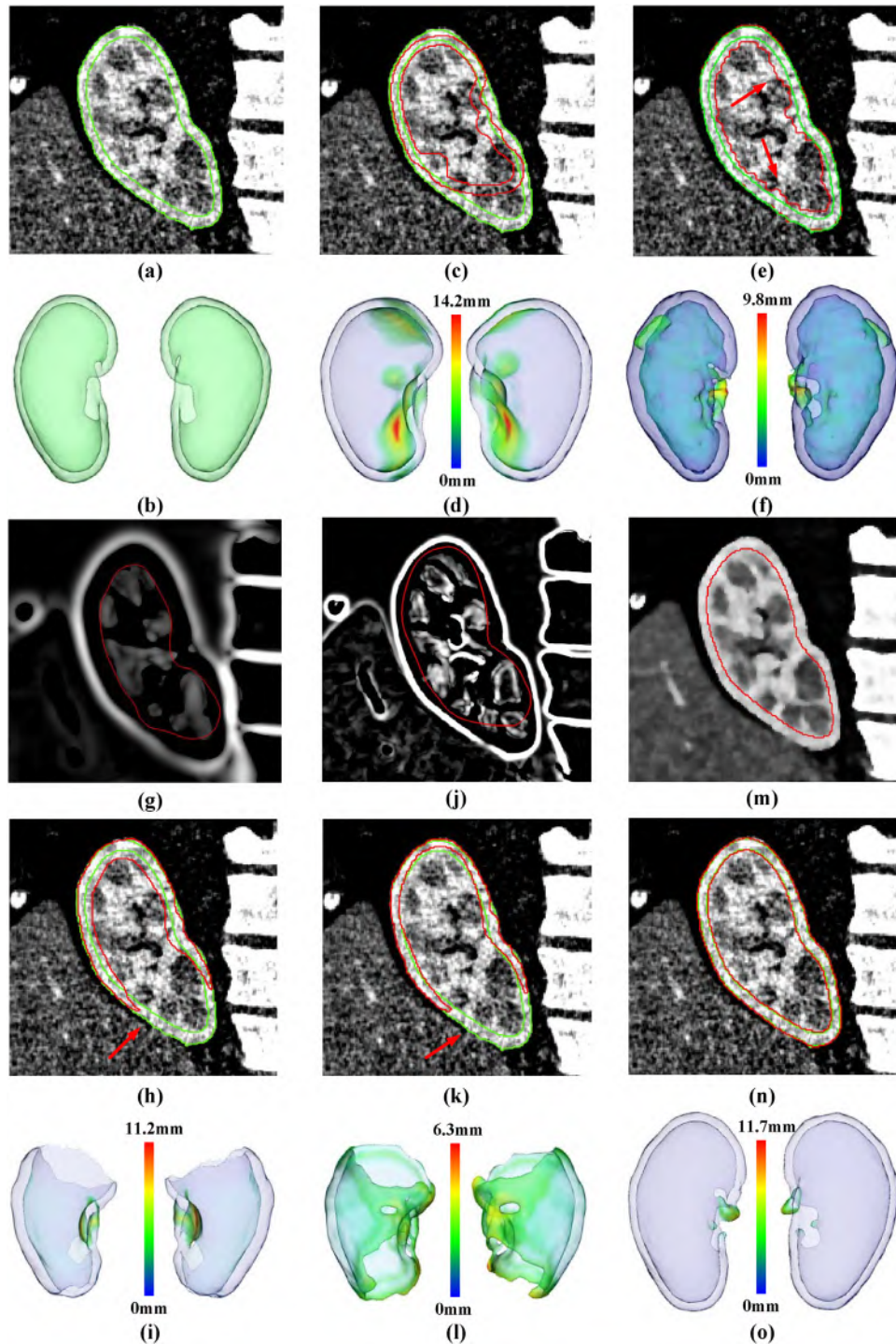


**Fig. 12.** Renal cortex segmentation (the green curve is reference segmentation and the red curve is the detected surface). (a) The original image in coronal view; (b) The 3D visualization of reference segmentation; (c) The initialized renal cortex; (d) The 3D visualization of surface distance between the initialized renal cortex and reference segmentation; (e) The renal cortex by using the random forest based method (Jin et al., 2016); (f) The 3D visualization of surface distance between the detected renal cortex by using the random forest based method (Jin et al., 2016) and reference segmentation; (g) The Hessian-based image ( $\sigma_s = 3.0$ ) and the inner surface by using traditional graph search method; (h) The original image and the detected renal cortex by using traditional graph search method; (i) The 3D visualization of surface distance between the detected renal cortex by using traditional graph search method and reference segmentation; (j) The Hessian-based image ( $\sigma_s = 1.0$ ) and the detected inner surface by using traditional graph search method; (k) The original image and the detected renal cortex by using traditional graph search method; (l) The 3D visualization of surface distance between the renal cortex by using traditional graph search method and reference segmentation; (m) The filtered image and the detected inner surface by using the proposed non-uniform graph search method; (n) The original image and the detected renal cortex by using the proposed non-uniform graph search method; (o) The 3D visualization of surface distance between the renal cortex by using the proposed non-uniform graph search method and reference segmentation. (For interpretation of the references to colour in this figure legend, the reader is referred to the web version of this article.)

**Table 2**

Quantitative results and comparative performance evaluation for renal cortex segmentation (mean  $\pm$  standard deviation). The bold numbers identify the best results.

Method	ASSD[mm]	ASRMSSD[mm]	SRVD[%]	VOE[%]	TPF[%]	FPF[%]	DSC[%]
Initialization	1.45 $\pm$ 0.80	2.37 $\pm$ 1.37	-13.01 $\pm$ 15.33	49.78 $\pm$ 11.32	62.04 $\pm$ 12.34	0.06 $\pm$ 0.03	66.06 $\pm$ 10.66
TGS( $\sigma_s = 3.0$ )	1.43 $\pm$ 0.60	2.46 $\pm$ 1.31	15.68 $\pm$ 22.47	42.75 $\pm$ 7.87	78.32 $\pm$ 11.21	0.10 $\pm$ 0.06	72.48 $\pm$ 6.57
Jin et al.	0.94 $\pm$ 0.31	1.83 $\pm$ 0.62	33.31 $\pm$ 15.52	31.20 $\pm$ 6.37	94.65 $\pm$ 4.85	0.09 $\pm$ 0.03	81.34 $\pm$ 4.63
TGS( $\sigma_s = 1.0$ )	0.86 $\pm$ 0.39	1.83 $\pm$ 0.82	<b>0.31 <math>\pm</math> 16.16</b>	30.74 $\pm$ 7.72	81.82 $\pm$ 9.15	0.05 $\pm$ 0.03	81.59 $\pm$ 5.44
Chen et al.	/	/	/	/	90.15 $\pm$ 3.11	0.85 $\pm$ 0.05	/
Li et al.	0.18 $\pm$ 0.11	0.80 $\pm$ 0.64	2.37 $\pm$ 1.72	<b>4.38 <math>\pm</math> 3.93</b>	/	/	90.50 $\pm$ 1.19
NUGS	<b>0.12 <math>\pm</math> 0.17</b>	<b>0.61 <math>\pm</math> 0.44</b>	2.52 $\pm$ 4.76	4.74 $\pm$ 5.61	<b>98.71 <math>\pm</math> 3.47</b>	<b>0.01 <math>\pm</math> 0.01</b>	<b>97.48 <math>\pm</math> 3.18</b>

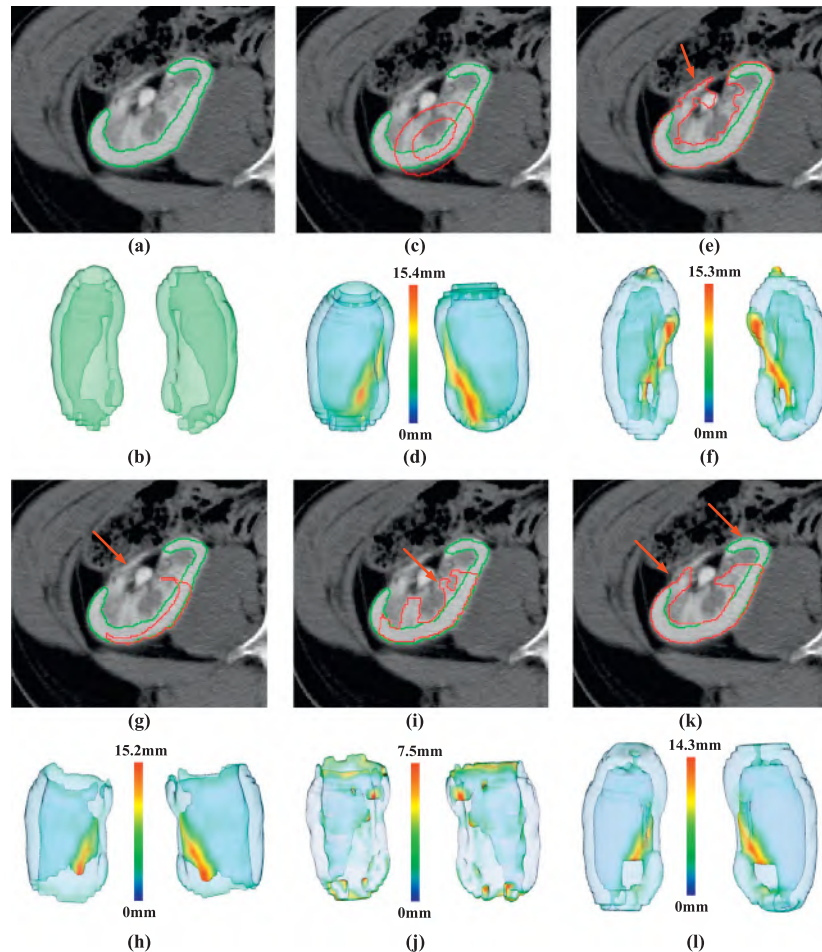


**Fig. 13.** A difficult case with large morphological change (the green curve is reference segmentation and the red curve is the detected surface). (a) Original image in axial view; (b) 3D visualization of the reference segmentation; (c) Initialized renal cortex; (d) 3D visualization of surface distances between the initialized renal cortex and reference segmentation; (e) Renal cortex by obtained using the random forest based method (Jin et al., 2016); (f) 3D visualization of surface distance between the renal cortex detected using the random forest based method (Jin et al., 2016) and the reference segmentation; (g) Original image and the detected renal cortex obtained using traditional graph search method ( $\sigma_s = 3.0$ ); (h) 3D visualization of surface distance between the renal cortex detected using traditional graph search method and reference segmentation ( $\sigma_s = 3.0$ ); (i) Original image and the renal cortex detected using traditional graph search method ( $\sigma_s = 1.0$ ); (j) 3D visualization of surface distance between the detected renal cortex by using traditional graph search method and the reference segmentation ( $\sigma_s = 1.0$ ); (k) Original image and the renal cortex detected using the proposed non-uniform graph search method; (l) 3D visualization of surface distances between the renal cortex obtained using the proposed non-uniform graph search method and the reference segmentation. (For interpretation of the references to colour in this figure legend, the reader is referred to the web version of this article.)

think that incorporating more parameters into the model may be a solution to address some of these problems. However, it is not a viable solution because including more parameter helping in such rare cases will unnecessarily increase the model complexity and cause over-fitting. Hence, in the current effort, the proposed system has a manual interaction tool for handling inaccurately segmented cases by allowing the users to correct the incorrect portion of the boundaries.

Recently, deep learning has attracted substantial attention of many researchers in medical image analysis due to its power-

ful learning representation of features at the low, mid, and high-levels. Although we are not aware of any particular deep learning scheme developed for renal cortex segmentation, we strongly believe that a convolutional neural network (CNN) carefully trained on a large number of image samples could reveal highly accurate and efficient segmentation results. However, it is important to note the current limitations of the deep learning methodologies in pixel-wise classification (i.e., segmentation) problems. The data augmentation and/or transfer learning are necessary to obtain reliable training of the CNN (Buty et al., 2016; Hussein et al.,

2017). Fine tuning with transfer learning maybe an option to address some of these difficulties pertaining to deep learning networks but fine-tuning, designing a suitable transfer learning, and completely 3D implementation of all these are not straightforward. Unlike well established computer vision tasks (i.e., ImageNET classification (Deng et al., 2009)), obtaining sufficiently large numbers of radiology images is not easy. This is indeed the case in our specific task.

Although we have presented a fair amount of data for evaluating our proposed method, it is highly desirable to further increase the numbers of available images for at least the following reasons: Creating a better model – this requirement is vital particularly if deep learning methods are to be considered. Unfortunately, contrast enhanced CT images for kidney diseases are not available in publicly available data sets. One major reason is that CT require ionizing radiation. Subsequently, it is difficult to form large-enough datasets of normal controls. Another reason is that the kidney disease prevalence in association with renal cortex is low. As a result, imaging data availability is limited.

## Acknowledgments

This work has been supported in part by the National Basic Research Program of China (973 Program) under Grant 2014CB748600, and in part by the National Natural Science Foundation of China (NSFC) under Grant 61401293, 81371629, 61401294, 81401451, 81401472. The authors thank to Prof. Xiaodong Wu for the great help to demonstrate the optimality of the proposed method.

## References

- Ali, A.M., Farag, A.A., El-Baz, A.S., 2007. Graph cuts framework for kidney segmentation with prior shape constraints. In: *Medical Image Computing and Computer-Assisted Intervention–MICCAI 2007*. Springer, pp. 384–392.
- Bagci, U., Chen, X., Udupa, J.K., 2012. Hierarchical scale-based multiobject recognition of 3-d anatomical structures. *Med. Imaging, IEEE Trans.* 31 (3), 777–789. doi:10.1109/TMI.2011.2180920.
- Boykov, Y., Kolmogorov, V., 2004. An experimental comparison of min-cut/max-flow algorithms for energy minimization in vision. *Pattern Anal. Mach. Intell. IEEE Trans.* 26 (9), 1124–1137.
- Boykov, Y., Lee, V.S., Rusinek, H., Bansal, R., 2001. Segmentation of dynamic nd data sets via graph cuts using Markov models. In: *Medical Image Computing and Computer-Assisted Intervention–MICCAI 2001*. Springer, pp. 1058–1066.
- Buty, M., Xu, Z., Gao, M., Bagci, U., Wu, A., Mollura, D.J., 2016. Characterization of lung nodule malignancy using hybrid shape and appearance features. In: *International Conference on Medical Image Computing and Computer-Assisted Intervention*. Springer, pp. 662–670.
- Chen, X., Summers, R.M., Cho, M., Bagci, U., Yao, J., 2012a. An automatic method for renal cortex segmentation on ct images: evaluation on kidney donors. *Acad. Radiol.* 19 (5), 562–570.
- Chen, X., Udupa, J.K., Alavi, A., Torigian, D.A., 2010a. Automatic anatomy recognition via multiobject oriented active shape models. *Med. Phys.* 37 (2), 6390–6401.
- Chen, X., Udupa, J.K., Bagci, U., Zhuge, Y., Yao, J., 2012b. Medical image segmentation by combining graph cuts and oriented active appearance models. *Image Process. IEEE Trans.* 21 (4), 2035–2046.
- Chen, X., Udupa, J.K., Zheng, X., Alavi, A., Torigian, D.A., 2009. Automatic anatomy recognition via multi-object-oriented active shape models. *SPIE Medical Imaging*. International Society for Optics and Photonics. pp. 72594P–72594P.
- Chen, X., Yao, J., Zhuge, Y., Bagci, U., 2010b. 3d automatic anatomy segmentation based on graph cut-oriented active appearance models. In: *Image Processing (ICIP), 2010 17th IEEE International Conference on*. IEEE, pp. 3653–3656.
- Chevallier, B., Ponvianne, Y., Collette, J.-L., Mandry, D., Claudon, M., Pietquin, O., 2008. Functional semi-automated segmentation of renal dce-mri sequences. In: *Acoustics, Speech and Signal Processing, 2008. ICASSP 2008. IEEE International Conference on*. IEEE, pp. 525–528.
- Clark, M.A., Shikanov, S., Raman, J.D., Smith, B., Kaag, M., Russo, P., Wheat, J.C., Wolf, J.S., Matin, S.F., Huang, W.C., et al., 2011. Chronic kidney disease before and after partial nephrectomy. *J. Urol.* 185 (1), 43–48.
- Davies, R.H., Twining, C.J., Cootes, T.F., Waterton, J.C., Taylor, C.J., 2002. A minimum description length approach to statistical shape modeling. *Med. Imaging, IEEE Trans.* 21 (5), 525–537.
- Deng, J., Dong, W., Socher, R., Li, L.-J., Li, K., Fei-Fei, L., 2009. Imagenet: a large-scale hierarchical image database. In: *Computer Vision and Pattern Recognition, 2009. CVPR 2009. IEEE Conference on*. IEEE, pp. 248–255.
- Dryden, I., Mardia, K., 1998. *Statistical Analysis of Shape*. Wiley.
- Ecabert, O., Peters, J., Schramm, H., Lorenz, C., von Berg, J., Walker, M.J., Vembar, M., Olszewski, M.E., Subramanian, K., Lavi, G., et al., 2008. Automatic model-based segmentation of the heart in ct images. *Med. Imaging, IEEE Trans.* 27 (9), 1189–1201.
- Ferlay, J., Soerjomataram, I., Ervik, M., Dikshit, R., Eser, S., Mathers, C., Rebelo, M., Parkin, D., Forman, D., Bray, F., 2013. Globocan 2012 v1.0. Cancer incidence and mortality worldwide: IARC CancerBase (11).
- Frangi, A., Niessen, W., Vincken, K., Viergever, M., 1998. Multiscale vessel enhancement filtering 1496, 130–137.
- Garcia, J.A., Cowey, C.L., Godley, P.A., 2009. Renal cell carcinoma. *Curr. Opin. Oncol.* 21 (3), 266–271.
- Garvin, M., Abramoff, M., Kardon, R., Russell, S., Wu, X., Sonka, M., 2008. Intraretinal layer segmentation of macular optical coherence tomography images using optimal 3-d graph search. *Med. Imaging, IEEE Trans.* 27 (10), 1495–1505. doi:10.1109/TMI.2008.923966.
- Heimann, T., van Ginneken, B., Styner, M.A., Arzhaeva, Y., Aurich, V., Bauer, C., Beck, A., Becker, C., Beichel, R., Bekes, G., et al., 2009. Comparison and evaluation of methods for liver segmentation from ct datasets. *Med. Imaging, IEEE Trans.* 28 (8), 1251–1265.
- Heimann, T., Oguz, I., Wolf, I., Styner, M., Meinzer, H.-P., 2006. Implementing the automatic generation of 3d statistical shape models with itk. *The Insight Journal MICCAI Open Science Workshop*, Copenhagen.
- Hoppe, H., 1999. New quadric metric for simplifying meshes with appearance attributes. In: *Proceedings of the conference on Visualization'99: celebrating ten years*. IEEE Computer Society Press, pp. 59–66.
- Horn, B.K., 1987. Closed-form solution of absolute orientation using unit quaternions. *JOSA A* 4 (4), 629–642.
- Hussein, S., Gillies, R., Cao, K., Song, Q., Bagci, U., 2017. Tumornet: lung nodule characterization using multi-view convolutional neural network with gaussian process. arXiv:1703.00645 arXiv preprint.
- Ibanez, L., Schroeder, W., Ng, L., Cates, J., 2005. *The itk software guide*.
- Jin, C., Shi, F., Xiang, D., Jiang, X., Zhang, B., Wang, X., Zhu, W., Gao, E., Chen, X., 2016. 3D fast automatic segmentation of kidney based on modified aam and random forest. *IEEE Trans. Med. Imaging* 35 (6), 1395–1407.
- Ju, W., Xiang, D., Zhang, B., Wang, L., Kopriva, I., Chen, X., 2015. Random walk and graph cut for co-segmentation of lung tumor on pet-ct images. *Image Process. IEEE Trans.* 24 (12), 5854–5867.
- Kato, F., Kamishima, T., Morita, K., Muto, N.S., Okamoto, S., Omatsu, T., Oyama, N., Terae, S., Kanegae, K., Nonomura, K., et al., 2011. Rapid estimation of split renal function in kidney donors using software developed for computed tomographic renal volumetry. *Eur. J. Radiol.* 79 (1), 15–20.
- Khoshelham, K., 2007. Extending generalized hough transform to detect 3d objects in laser range data. *ISPRS Workshop on Laser Scanning and SilviLaser 2007, 12–14 September 2007*, Espoo, Finland. International Society for Photogrammetry and Remote Sensing.
- Li, G., Chen, X., Shi, F., Zhu, W., Tian, J., Xiang, D., 2015. Automatic liver segmentation based on shape constraints and deformable graph cut in ct images. *Image Process. IEEE Trans.* 24 (12), 5315–5329.
- Li, K., Wu, X., Chen, D., Sonka, M., 2006. Optimal surface segmentation in volumetric images—a graph-theoretic approach. *Pattern Anal. Mach. Intell. IEEE Trans.* 28 (1), 119–134. doi:10.1109/TPAMI.2006.19.
- Li, X., Chen, X., Yao, J., Zhang, X., Yang, F., Tian, J., 2012. Automatic renal cortex segmentation using implicit shape registration and novel multiple surfaces graph search. *Med. Imaging, IEEE Trans.* 31 (10), 1849–1860.
- Lorenson, W.E., Cline, H.E., 1987. Marching cubes: a high resolution 3d surface construction algorithm. In: *ACM siggraph computer graphics*, 21. ACM, pp. 163–169.
- Meijster, A., Roerdink, J.B.T.M., Hesselink, W.H., 2000. A general algorithm for computing distance transforms in linear time. In: *Mathematical Morphology and its Applications to Image and Signal Processing*. Kluwer Acad. Publ., pp. 331–340.
- Muto, N.S., Kamishima, T., Harris, A.A., Kato, F., Onodera, Y., Terae, S., Shirato, H., 2011. Renal cortical volume measured using automatic contouring software for computed tomography and its relationship with bmi, age and renal function. *Eur. J. Radiol.* 78 (1), 151–156.
- Padigala, K.K., Hartle, J.E., Kirchner, H.L., Schultz, M.F., 2009. Renal cortical thickness as a predictor of renal function and blood pressure status post renal artery stenting. *Angiology* 60 (6), 719–724.
- de Priester, J.A., Kessels, A.G., Giele, E.L., den Boer, J.A., Christiaans, M.H., Hasman, A., van Engelshoven, J., 2001. Mr renography by semiautomated image analysis: performance in renal transplant recipients. *J. Magn. Reson. Imaging* 14 (2), 134–140.
- Rusinek, H., Boykov, Y., Kaur, M., Wong, S., Bokacheva, L., Sajous, J.B., Huang, A.J., Heller, S., Lee, V.S., 2007. Performance of an automated segmentation algorithm for 3d mr renography. *Magn. Reson. Med.* 57 (6), 1159–1167.
- Russo, P., Huang, W., 2008. The medical and oncological rationale for partial nephrectomy for the treatment of t1 renal cortical tumors. *Urologic Clin. North Am.* 35 (4), 635–643.
- Shao, P., Tang, L., Li, P., Xu, Y., Qin, C., Cao, Q., Ju, X., Meng, X., Lv, Q., Li, J., et al., 2012. Precise segmental renal artery clamping under the guidance of dual-source computed tomography angiography during laparoscopic partial nephrectomy. *Eur. Urol.* 62 (6), 1001–1008.
- Shen, W., Kassim, A.A., Koh, H., Shuter, B., 2009. Segmentation of kidney cortex in mri studies: a constrained morphological 3d h-maxima transform approach. *Int. J. Med. Eng. Inf.* 1 (3), 330–341.
- Shim, H., Chang, S., Tao, C., Wang, J.H., Kaya, D., Bae, K.T., 2009. Semiautomated

- segmentation of kidney from high-resolution multidetector computed tomography images using a graph-cuts technique. *J. Comput. Assisted Tomogr.* 33 (6), 893–901.
- Song, T., Lee, V.S., Rusinek, H., Bokacheva, L., Laine, A., 2008. Segmentation of 4d mr renography images using temporal dynamics in a level set framework. In: *Biomedical Imaging: From Nano to Macro, 2008. ISBI 2008. 5th IEEE International Symposium on*. IEEE, pp. 37–40.
- Sun, Y., Jolly, M.-P., Moura, J., 2004. Integrated registration of dynamic renal perfusion mr images. In: *Image Processing, 2004. ICIP'04. 2004 International Conference on*, 3. IEEE, pp. 1923–1926.
- Tang, Y., Jackson, H.A., De Filippo, R.E., Nelson, M.D., Moats, R.A., 2010. Automatic renal segmentation applied in pediatric mr urography. *Int. J. Intell. Inf. Process.* 1 (1).
- Whitaker, R.T., Xue, X., 2001. Variable-conductance, level-set curvature for image denoising. In: *Image Processing, 2001. Proceedings. 2001 International Conference on*, 3. IEEE, pp. 142–145.
- Xiang, D., Tian, J., Yang, F., Yang, Q., Zhang, X., Li, Q., Liu, X., 2011. Skeleton cutlan efficient segmentation method for volume rendering. *Visual Comput. Graphics, IEEE Trans.* 17 (9), 1295–1306.
- Yano, M., Lin, M.F., Hoffman, K.A., Vijayan, A., Pilgram, T.K., Narra, V.R., 2012. Renal measurements on ct angiograms: correlation with graft function at living donor renal transplantation. *Radiology* 265 (1), 151–157.
- Yin, Y., Zhang, X., Williams, R., Wu, X., Anderson, D.D., Sonka, M., 2010. LOGIS-MOS-layered optimal graph image segmentation of multiple objects and surfaces: cartilage segmentation in the knee joint. *Med. Imaging, IEEE Trans.* 29 (12), 2023–2037.
- Zöllner, F.G., Sance, R., Rogelj, P., Ledesma-Carbayo, M.J., Rørvik, J., Santos, A., Lunderdold, A., 2009. Assessment of 3d dce-mri of the kidneys using non-rigid image registration and segmentation of voxel time courses. *Computerized Med. Imaging Graphics* 33 (3), 171–181.